Imaging a moving point source from multi-frequency data measured at one and sparse observation points (part II): near-field case in 3D

Guanqiu Ma[†], Hongxia Guo[*,†], Guanghui Hu[†]

Abstract

In this paper we propose a frequency-domain method for recovering the trajectory of a moving point source from multi-frequency near-field data measured at one and sparse observation points in three dimensions. The radiating period of the moving point source is supposed to be supported on the real axis and a priori known. In contrast to inverse stationary source problems, one needs to study observable and non-observable measurement positions. The analogue of these concepts in the far-field regime were firstly proposed in the authors' previous paper (to appear in SIAM J. Imaging Sciences, 2023). In this paper the observable and non-observable measurement positions for straight and circular motions are analyzed. In the near-field case, we verify that the smallest annular region that contains the trajectory and centered at an observable position can be imaged for an admissible class of orbit functions. Using the data from sparse observable positions, it is possible to reconstruct the Θ-convex domain of the trajectory. Intensive 3D numerical tests with synthetic data are performed to show effectiveness and feasibility of this new algorithm.

Keywords: **inverse moving source problem, Helmholtz equation, multi-frequency data, factorization method, uniqueness, near-field data**

1 Introduction

1.1 Time-dependent model and its Fourier transform

We suppose that the whole space $\mathbb{R}^3$ is filled with a homogeneous and isotropic medium with a unit mass density. Consider a moving point source along the trajectory function $a(t) : [t_{\min}, t_{\max}] \to \mathbb{R}^3 \in C^1[t_{\min}, t_{\max}]$ with $0 < t_{\min} < t_{\max}$. The source function S is supposed to radiate wave signals at the beginning time $t_{\min}$ and stop radiating at the time point $t_{\max}$, i.e.,

[*]Corresponding author

[†]School of Mathematical Sciences and LPMC, Nankai University, Tianjin, 300071, China(gqma@nankai.edu.cn, hxguo_math@163.com, ghhu@nankai.edu.cn).

it is supported in the interval $[t_{\min}, t_{\max}]$ with respect to the time variable $t > 0$. Hence, the source function takes the form

$$S(x,t) = \delta(x - a(t))g(t)\chi(t), \tag{1.1}$$

where δ denotes the Dirac delta function, $g(t) \in C(t_{\min}, t_{\max})$ is a real-valued function fulfilling the coercivity constraint

$$|g(t)| \geq c_0 > 0, \quad t \in [t_{\min}, t_{\max}], \tag{1.2}$$

and

$$\chi(t) = \begin{cases} 1, & t \in [t_{\min}, t_{\max}], \\ 0, & t \notin [t_{\min}, t_{\max}], \end{cases}$$

is the characteristic function over the interval $[t_{\min}, t_{\max}]$. Denote the trajectory by $\Gamma \coloneqq \{x : x = a(t),\, t \in [t_{\min}, t_{\max}]\}$. One can easily find Supp $S(\cdot, t) \subset \Gamma$ for all $t \in [t_{\min}, t_{\max}]$. The propagation of the radiated wave fields $U(x,t)$ is governed by the initial value problem

$$\begin{cases} \dfrac{\partial^2 U}{\partial t^2} = \Delta U + S(x,t), & (x,t) \in \mathbb{R}^3 \times \mathbb{R}^+, \mathbb{R}^+ \coloneqq \{t \in \mathbb{R} : t > 0\}, \\ U(x,0) = \partial_t U(x,0) = 0, & x \in \mathbb{R}^3. \end{cases} \tag{1.3}$$

The solution U can be written explicitly as the convolution of the fundamental solution G to the wave equation with the source term,

$$U(x,t) = G(x;t) * S(x,t) \coloneqq \int_{\mathbb{R}^+} \int_{\mathbb{R}^3} G(x-y; t-\tau) S(y,\tau)\, dy d\tau \tag{1.4}$$

where

$$G(x;t) = \frac{\delta(t - |x|)}{4\pi |x|}.$$

In this paper the one-dimensional Fourier and inverse Fourier transforms are defined by

$$(\mathcal{F}u)(k) = \frac{1}{\sqrt{2\pi}} \int_{\mathbb{R}} u(t) e^{-ikt}\, dt, \quad (\mathcal{F}^{-1}v)(t) = \frac{1}{\sqrt{2\pi}} \int_{\mathbb{R}} v(k) e^{ikt}\, dk,$$

respectively. The Fourier transform of S is thus given by

$$f(x,k) \coloneqq (\mathcal{F}S(x,\cdot))(k) = \frac{1}{\sqrt{2\pi}} \int_{\mathbb{R}} \delta(x - a(t)) g(t) \chi(t) e^{-ikt}\, dt = \frac{1}{\sqrt{2\pi}} \int_{t_{\min}}^{t_{\max}} \delta(x - a(t)) g(t) e^{-ikt}\, dt. \tag{1.5}$$

It is obvious $f(x,k) = 0$ for all $x \notin \Gamma$ and $k \in [k_{\min}, k_{\max}]$. From the expression (1.4), one deduces the Fourier transform of the wave fields U,

$$\begin{aligned} w(x,k) = (\mathcal{F}U)(x,k) &= \int_{\mathbb{R}^3} (\mathcal{F}G)(x-y;k)(\mathcal{F}S)(y,k)\, dy \\ &= \frac{1}{\sqrt{2\pi}} \int_{\mathbb{R}^3} \Phi(x-y;k) f(y,k)\, dy. \end{aligned} \tag{1.6}$$

Here, $\Phi(x-y;k)$ is the fundamental solution to the Helmholtz equation $(\Delta+k^2)w=0$, given by

$$\Phi(x-y;k)=\frac{e^{ik|x-y|}}{4\pi|x-y|},\quad x\neq y,\ x,y\in\mathbb{R}^3,$$

and $H_0^{(1)}$ is the Hankel function of the first kind of order zero. On the other hand, taking the Fourier transform on the wave equation yields the inhomogeneous Helmholtz equations

$$\Delta w(x,k)+k^2w(x,k)=-f(x,k),\qquad x\in\mathbb{R}^3,\ k>0. \tag{1.7}$$

From (1.6) we observe that w satisfies the Sommerfeld radiation condition

$$\lim_{r\to\infty} r(\partial_r w-ikw)=0,\quad r=|x|, \tag{1.8}$$

which holds uniformly in all points $x\in\mathbb{R}^3$.

1.2 Formulation in the frequency domain and literature review

Denote by $[k_{\min},k_{\max}]$ an interval of frequencies on the positive real axis. From the time-domain setting we see

$$f(x,k)\neq 0,\ x\in\Gamma,\quad f(x,k)=0,\ x\notin\Gamma$$

for all $k\in[k_{\min},k_{\max}]$, implying supp $f(\cdot,k)=\Gamma$ for all $k\in[k_{\min},k_{\max}]$. For every $k>0$, the unique solution $w\in H^2_{loc}(\mathbb{R}^3)$ to (1.7)-(1.8) is given by (1.6), i.e.,

$$w(x,k)=\frac{1}{\sqrt{2\pi}}\int_{\mathbb{R}^3}\Phi(x-y;k)f(y,k)dy=\frac{1}{8\pi^2}\int_{t_{\min}}^{t_{\max}}\frac{e^{-ik(t-|x-a(t)|)}}{|x-a(t)|}g(t)\,dt,\quad x\notin\Gamma. \tag{1.9}$$

Noting that the time-dependent source S is real valued, we have $f(x,-k)=\overline{f(x,k)}$ for all $k>0$ and thus $w(x,-k)=\overline{w(x,k)}$.

In this paper we are interested in the following inverse problem (see Fig. 1):

(IP): Recovery the trajectory Γ from knowledge of the multi-frequency near-field patterns

$$\{w(x_j,k):k\in[k_{\min},k_{\max}],\ j=1,2,\cdots,M\}.$$

where $x_j\in S_R:=\{x:|x|=R\}$ are sparse observation points and $[k_{\min},k_{\max}]$ denotes a broad band of frequencies. Here we assume $R>\sup\limits_{t\in[t_{\min},t_{\max}]}|a(t)|$.

In particular, we are interested the following question:

What kind information on Γ can be extracted from the the multi-frequency near-field data $\{w(x,k):k\in[k_{\min},k_{\max}]\}$ at a fixed observation point $x\in S_R$?

The above questions are of great importance in industrial, medical and military applications, because the number the measurement positions is usually quite limited and multi-frequency data are always available by Fourier transforming the time-dependent measurement data.

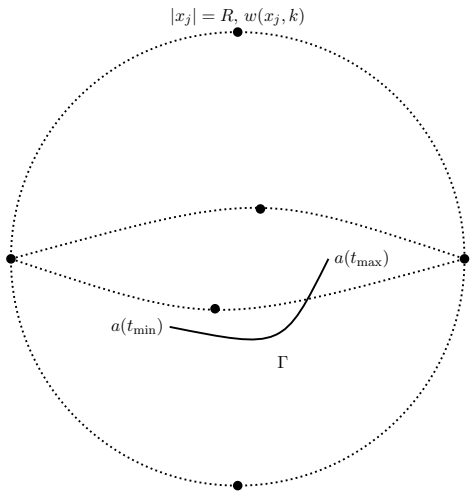

Figure 1: Imaging the trajectory Γ from knowledge of multi-frequency near-field patterns measured at sparse observation points $|x_j| = R$, $j = 1, 2, \ldots, M$.

2 Factorization of near-field operator

The aim of this section is to explore the factorization method for recovering the trajectory $\Gamma = \mathrm{Supp} f(\cdot, k)$ from the data measured at a single observation point $x \in S_R$. We shall proceed with the lines of [9] to derive a factorization of the near-field operator $\mathcal{N}^{(x)}$. Following the spirit of [8], we introduce the central frequency κ and half of the bandwidth of the given data K as

$$\kappa := \frac{k_{\min} + k_{\max}}{2}, \quad K := \frac{k_{\max} - k_{\min}}{2}.$$

Define the near-field operator $\mathcal{N}^{(x)} : L^2(0, K) \to L^2(0, K)$ by

$$(\mathcal{N}^{(x)}\phi)(\tau) := \int_0^K w(x, \kappa + \tau - s)\, \phi(s)\, ds, \qquad \tau \in (0, K). \tag{2.10}$$

Recall from (1.9) that w is analytic in $k \in \mathbb{R}$. Hence the near-field operator $\mathcal{N}^{(x)}$ is linear and bounded. Further, it holds that

$$\begin{aligned}
(\mathcal{N}^{(x)}\phi)(\tau) &= \int_0^K \frac{1}{\sqrt{2\pi}} \int_{\mathbb{R}^3} \Phi(x - y; \kappa + \tau - s) f(y, \kappa + \tau - s)\, dy\, \phi(s)\, ds \\
&= \frac{1}{\sqrt{2\pi}} \int_0^K \int_{\mathbb{R}^3} \frac{e^{i(\kappa+\tau-s)|x-y|}}{4\pi|x-y|} \left(\frac{1}{\sqrt{2\pi}} \int_{t_{\min}}^{t_{\max}} e^{-i(\kappa+\tau-s)t} \delta(y - a(t)) g(t)\, dt \right) dy\, \phi(s)\, ds \\
&= \frac{1}{2\pi} \int_0^K \int_{t_{\min}}^{t_{\max}} \frac{e^{-i(\kappa+\tau-s)(t-|x-a(t)|)}}{4\pi|x - a(t)|} g(t)\, dt\, \phi(s)\, ds
\end{aligned} \tag{2.11}$$

Below we shall prove a factorization of the above near-field operator.

Theorem 2.1. *We have $\mathcal{N}^{(x)} = \mathcal{L}\mathcal{T}\mathcal{L}^*$ where $\mathcal{L} = \mathcal{L}^{(x)} : L^2(t_{\min}, t_{\max}) \to L^2(0, K)$ is defined by*

$$(\mathcal{L}\psi)(\tau) \coloneqq \int_{t_{\min}}^{t_{\max}} e^{-i\tau(t-|x-a(t)|}\psi(t)\,dt, \quad \tau \in (0, K) \tag{2.12}$$

for all $\psi \in L^2(t_{\min}, t_{\max})$. Here the middle operator $\mathcal{T} : L^2(t_{\min}, t_{\max}) \to L^2(t_{\min}, t_{\max})$ is a multiplication operator defined by

$$(\mathcal{T}\varphi)(t) \coloneqq \frac{e^{-i\kappa(t-|x-a(t)|)}}{8\pi^2|x-a(t)|} g(t)\varphi(t). \tag{2.13}$$

Remark 2.2. *In the remaining part of this paper the operator $\mathcal{L}$ will be referred to as the data-to-pattern operator corresponding to the orbit function $a(t)$. It is obvious that the near-field data (1.9) can be expressed as $w(x,k) = (\mathcal{L}^{(x)} \frac{1}{8\pi^2|x-a(t)|})(k)$.*

Proof. We first show that the adjoint operator $\mathcal{L}^* : L^2(0, K) \to L^2(t_{\min}, t_{\max})$ of $\mathcal{L}$ can be expressed by

$$(\mathcal{L}^*\phi)(t) \coloneqq \int_0^K e^{is(t-|x-a(t)|)}\phi(s)\,ds, \quad \phi \in L^2(0, K). \tag{2.14}$$

Indeed, for $\psi \in L^2(t_{\min}, t_{\max})$ and $\phi \in L^2(0, K)$, it holds that

$$\begin{aligned}
\langle \mathcal{L}\psi, \phi\rangle_{L^2(0,K)} &= \int_0^K \left(\int_{t_{\min}}^{t_{\max}} e^{-i\tau(t-|x-a(t)|)}\psi(t)\,dt \right) \overline{\phi(\tau)}\,d\tau \\
&= \int_{t_{\min}}^{t_{\max}} \psi(t) \left(\int_0^K \overline{e^{i\tau(t-|x-a(t)|)}\phi(\tau)} d\tau \right) dt \\
&= \langle \psi, \mathcal{L}^*\phi\rangle_{L^2(t_{\min}, t_{\max})}.
\end{aligned}$$

which implies (2.14). By the definition of $\mathcal{T}$, we have

$$(\mathcal{T}\mathcal{L}^*\phi)(t) = \frac{e^{-i\kappa(t-|x-a(t)|)}}{8\pi^2|x-a(t)|} g(t) \int_0^K e^{is(t-|x-a(t)|)}\phi(s)\,ds, \quad \phi \in L^2(0, K).$$

Hence, using (1.5) and (2.11),

$$\begin{aligned}
(\mathcal{L}\mathcal{T}\mathcal{L}^*\phi)(\tau) &= \int_{t_{\min}}^{t_{\max}} e^{-i\tau(t-|x-a(t)|)} \left(\frac{e^{-i\kappa(t-|x-a(t)|)}}{8\pi^2|x-a(t)|} g(t) \int_0^K e^{is(t-|x-a(t)|)}\phi(s)\,ds \right) dt \\
&= \frac{1}{2\pi} \int_0^K \int_{t_{\min}}^{t_{\max}} \frac{e^{-i(\kappa+\tau-s)(t-|x-a(t)|)}}{4\pi|x-a(t)|} g(t)\,dt\,\phi(s)\,ds \\
&= (\mathcal{N}^{(x)}\phi)(\tau).
\end{aligned}$$

This proves the factorization $\mathcal{N}^{(x)} = \mathcal{L}\mathcal{T}\mathcal{L}^*$. □

Denote by Range($\mathcal{L}^{(x)}$) the range of the data-to-pattern operator $\mathcal{L} = \mathcal{L}^{(x)}$ (see (2.12)) acting on $L^2(t_{\min}, t_{\max})$.

Lemma 2.3. *The operator $\mathcal{L} : L^2(t_{\min}, t_{\max}) \to L^2(0, K)$ is compact with dense range.*

Proof. For any $\psi \in L^2(t_{\min}, t_{\max})$, it holds that $\mathcal{L}\psi \in H^1(0,K)$, which is compactly embedded into $L^2(0,K)$. This proves the compactness of $\mathcal{L}$. By (2.14), $(\mathcal{L}^*\phi)(t)$ coincides with the inverse Fourier transform of ϕ at the variable $t-|x-a(t)|$. Since the set $\{t-|x-a(t)| : t \in [t_{\min}, t_{\max}]\}$ forms an interval of $\mathbb{R}$, the relation $(\mathcal{L}^*\phi)(t) = 0$ implies $\phi = 0$ in $L^2(0,K)$. Hence, $\mathcal{L}^*$ is injective. The denseness of Range$(\mathcal{L}^{(x)})$ in $L^2(0,K)$ follows from the injectivity of $\mathcal{L}^*$. □

Within the framework of Factorization method, it is essential to connect the ranges of $\mathcal{N}^{(x)}$ and $\mathcal{L}$. We first recall that, for a bounded operator $F : Y \to Y$ in a Hilbert space Y the real and imaginary parts of F are defined respectively by

$$\operatorname{Re} F = \frac{F+F^*}{2}, \quad \operatorname{Im} F = \frac{F-F^*}{2i},$$

which are both self-adjoint operators. Furthermore, by spectral representation we define the self-adjoint and positive operator $|\operatorname{Re} F|$ as

$$|\operatorname{Re} F| = \int_{\mathbb{R}} |\lambda| \, dE_\lambda, \qquad \text{if} \quad \operatorname{Re} F = \int_{\mathbb{R}} \lambda \, dE_\lambda.$$

The selfadjoint and positive operator $|\operatorname{Im} F|$ can be defined analogously. Introduce a new operator

$$F_\# := |\operatorname{Re} F| + |\operatorname{Im} F|.$$

Since $F_\#$ is selfadjoint and positive, its square root $F_\#^{1/2}$ is defined as

$$F_\#^{1/2} := \int_{\mathbb{R}^+} \sqrt{\lambda} \, dE_\lambda, \qquad \text{if} \quad F_\# = \int_{\mathbb{R}^+} \lambda \, dE_\lambda.$$

In this paper we need the following result from functional analysis.

Theorem 2.4. *([9]) Let X and Y be Hilbert spaces and let $F : Y \to Y$, $L : X \to Y$, $T : X \to X$ be linear bounded operators such that $F = LTL^*$. We make the following assumptions*

(i) L is compact with dense range and thus L^* is compact and one-to-one.

(ii) $\operatorname{Re} T$ and $\operatorname{Im} T$ are both one-to-one, and the operator $T_\# = |\operatorname{Re} T| + |\operatorname{Im} T| : X \to X$ is coercive, i.e., there exists $c > 0$ with

$$\langle T_\# \varphi, \varphi \rangle \geq c \, ||\varphi||^2 \quad \text{for all} \quad \varphi \in X.$$

Then the operator $F_\#$ is positive and the ranges of $F_\#^{1/2} : Y \to Y$ and $L : X \to Y$ coincide.

To apply Theorem 2.4 to our inverse problem, we set

$$F = \mathcal{N}^{(x)}, \quad L = \mathcal{L}, \quad T = \mathcal{T}, \quad X = L^2(t_{\min}, t_{\max}), \quad Y = L^2(0,K),$$

where $\mathcal{T}$ is the multiplication operator of (2.13). It is easy to see

$$\begin{aligned}[(\mathrm{Re}\,\mathcal{T})\,\varphi](t) &= \frac{\cos[\kappa(t-|x-a(t)|)]}{8\pi^2|x-a(t)|}g(t)\varphi(t),\\ [(\mathrm{Im}\,\mathcal{T})\,\varphi](t) &= -\frac{\sin[\kappa(t-|x-a(t)|)]}{8\pi^2|x-a(t)|}g(t)\varphi(t)\end{aligned}$$

are both one-to-one operators from $L^2(t_{\min}, t_{\max})$ onto $L^2(t_{\min}, t_{\max})$. The coercivity assumption of $\mathcal{N}^{(x)}$ yields the coercivity of $\mathcal{T}_{\#}$. As a consequence of Theorem 2.4, we obtain

$$\mathrm{Range}\,[(\mathcal{N}^{(x)})_{\#}^{1/2}] = \mathrm{Range}\,(\mathcal{L}^{(x)}) \quad \text{for any } x \in S_R. \tag{2.15}$$

Let $\varphi \in L^2(0,K)$ be a test function. We want to characterize the range of $\mathcal{L}^{(x)}$ through the choice of φ. Denote by $(\lambda_n^{(x)}, \psi_n^{(x)})$ an eigensystem of the positive and self-adjoint operator $(\mathcal{N}^{(x)})_{\#}$, which is uniquely determined by the multi-frequency near-field patterns $\{w(x,k) : k \in (k_{\min}, k_{\max})\}$. Applying Picard's theorem and Theorem 2.4, we obtain

$$\varphi \in \mathrm{Range}(\mathcal{L}^{(x)}) \quad \text{if and only if} \quad \sum_{n=1}^{\infty} \frac{|\langle \varphi, \psi_n^{(x)}\rangle|^2}{|\lambda_n^{(x)}|} < +\infty. \tag{2.16}$$

To establish the factorization method, we now need to choose a proper class of test functions which usually rely on a sample variable in $\mathbb{R}^3$.

3 Range of $\mathcal{L}^{(x)}$ and test functions

To characterize the range of $\mathcal{L}^{(x)}$, we need to investigate monotonicity of the function $\xi = h(t) := t - |x - a(t)| \in C^1[t_{\min}, t_{\max}]$. For this purpose we define the division points of a continuous function over a closed interval.

Definition 3.1. *Let $f \in C[t_{\min}, t_{\max}]$. The point $t \in (t_{\min}, t_{\max})$ is called a division point if*
(1) $f(t) = 0$;
(2) There exist an $\epsilon_0 > 0$ such that either $|f(t+\epsilon)| > 0$ or $|f(t-\epsilon)| > 0$ for all $0 < \epsilon < \epsilon_0$.

Obviously, the division points constitute a subset of the zero set of a continuous function. However, a division point cannot be an interior point of the zero set. Since $a(t) \in C^1[t_{\min}, t_{\max}]$, there are finitely many division points of the function h', which we denote by $t_1 < t_2 < \cdots < t_{n-1}$. The interval $[t_{\min}, t_{\max}]$ is then divided into n sub-intervals $[t_{j-1}, t_j]$, $j = 1, 2, \cdots, n$, where $t_{\min} = t_0$ and $t_{\max} = t_n$. Let a_j and h_j be the restrictions of a and h to $[t_{j-1}, t_j]$, respectively. Set

$$\xi_{j,\min}^{(x)} := \inf_{t\in[t_{j-1},t_j]}\{h_j(t)\}, \quad \xi_{j,\max}^{(x)} := \sup_{t\in[t_{j-1},t_j]}\{h_j(t)\}, \quad j = 1, 2, \cdots n.$$

In each subinterval (t_{j-1}, t_j), one of following cases must hold:

- $h_j'(t) > 0$ for all $t \in (t_{j-1}, t_j)$. There holds

$$\xi_{j,\min}^{(x)} = t_{j-1} - |x - a_j(t_{j-1})|, \quad \xi_{j,\max}^{(x)} = t_j - |x - a_j(t_j)|;$$

- $h_j'(t) < 0$ for all $t \in (t_{j-1}, t_j)$. We have

$$\xi_{j,\min}^{(x)} = t_j - |x - a_j(t_j)|, \quad \xi_{j,\max}^{(x)} = t_{j-1} - |x - a_j(t_{j-1})|;$$

- $h_j'(t) = 0$ for all $t \in (t_{j-1}, t_j)$. Consequently,

$$\xi_{j,\min}^{(x)} = \xi_{j,\max}^{(x)} = t - |x - a_j(t)|, \quad t \in [t_{j-1}, t_j].$$

Define

$$\xi_{\min}^{(x)} := \min_j \xi_{j,\min}^{(x)} = \inf_{t \in [t_{\min}, t_{\max}]} \{h(t)\}, \quad \xi_{\max}^{(x)} := \max_j \xi_{j,\max}^{(x)} = \sup_{t \in [t_{\min}, t_{\max}]} \{h(t)\}, \tag{3.17}$$

which denote the minimum and maximum of h over $[t_{\min}, t_{\max}]$, respectively. If $|h_j'(t)| > 0$, the monotonicity of the function $\xi = h_j(t)$ for $t \in [t_j, t_{j-1}]$ implies the inverse function $t = h_j^{-1}(\xi) \in C^1[\xi_{j,\min}^{(x)}, \xi_{j,\max}^{x)}]$. Set

$$J = \{j \in \mathbb{N} : 1 \le j \le n, h_j'(t) \equiv 0, t \in (t_{j-1}, t_j)\}.$$

and assume $h_j(t) \equiv c_j \in \mathbb{R}$ for $j \in J$. Note that it is possible that $J = \emptyset$.

With these notations we can rephrase the operator $\mathcal{L}^{(x)}$ defined by (2.12) as

$$\begin{aligned} (\mathcal{L}^{(x)}\psi)(\tau) &= \sum_{j=1}^{n} \int_{t_{j-1}}^{t_j} e^{-i\tau h_j(t)} \psi(t)\, dt \\ &= \sum_{j \notin J} \int_{t_{j-1}}^{t_j} e^{-i\tau h_j(t)} \psi(t)\, dt + \sum_{j \in J} e^{-i\tau c_j} \int_{t_{j-1}}^{t_j} \psi(t)\, dt. \end{aligned} \tag{3.18}$$

For $j \in J$, using $e^{-i\tau c} = \sqrt{2\pi}\mathcal{F}\delta(t - c)$ we can rewrite each term in the second sum as

$$e^{-i\tau c_j} \int_{t_{j-1}}^{t_j} \psi(t)\, dt = \sqrt{2\pi}\mathcal{F}\delta(t - c_j) \int_{t_{j-1}}^{t_j} \psi(t)\, dt. \tag{3.19}$$

For $j \notin J$ and $h_j'(t) > 0$, the integral in the first summation on the right hand of (3.18) takes the form

$$\begin{aligned} \int_{t_{j-1}}^{t_j} e^{-i\tau h_j(t)} \psi(t)\, dt &= \int_{\xi_{j,\min}^{(x)}}^{\xi_{j,\max}^{(x)}} e^{-i\tau\xi} \psi(h_j^{-1}(\xi))\, (h_j^{-1}(\xi))'\, d\xi \\ &= \int_{\xi_{j,\min}^{(x)}}^{\xi_{j,\max}^{(x)}} e^{-i\tau\xi} \psi(h_j^{-1}(\xi)) |(h_j^{-1}(\xi))'|\, d\xi. \end{aligned}$$

Note that $[h_j^{-1}(\xi)]' > 0$, due to the relation $h_j'(t)[h_j^{-1}(\xi)]' = 1$. Analogously, if $h_j'(t) < 0$ for some $j \notin J$, we have $[h_j^{-1}(\xi)]' < 0$ and thus

$$\begin{aligned}\int_{t_{j-1}}^{t_j} e^{-i\tau h_j(t)}\psi(t)\,dt &= -\int_{\xi_{j,\min}^{(x)}}^{\xi_{j,\max}^{(x)}} e^{-i\tau\xi}\psi(h_j^{-1}(\xi))(h_j^{-1}(\xi))'\,d\xi \\ &= \int_{\xi_{j,\min}^{(x)}}^{\xi_{j,\max}^{(x)}} e^{-i\tau\xi}\psi(h_j^{-1}(\xi))|(h_j^{-1}(\xi))'|\,d\xi.\end{aligned}$$

Now, extending h_j^{-1} by zero from $(\xi_{j,\min}^{(x)}, \xi_{j,\max}^{(x)})$ to $\mathbb{R}$ and extending $\psi \in L^2(t_{\min}, t_{\max})$ by zero to $L^2(\mathbb{R})$, we can write each term for $j \notin J$ as

$$\int_{t_{j-1}}^{t_j} e^{-i\tau h_j(t)}\psi(t)\,dt = \int_{\mathbb{R}} e^{-i\tau\xi}\psi(h_j^{-1}(\xi))|(h_j^{-1}(\xi))'|\,d\xi. \tag{3.20}$$

Combining (3.18), (3.19) and (3.20), we get

$$(\mathcal{L}^{(x)}\psi)(\tau) = \int_{\mathbb{R}} e^{-i\tau\xi} g(\xi)\,d\xi, \tag{3.21}$$

with

$$g(\xi) = \sum_{j\notin J} \psi(h_j^{-1}(\xi))\,|(h_j^{-1}(\xi))'| + \sum_{j\in J} \delta(\xi - c_j)\int_{t_{j-1}}^{t_j} \psi(t)\,dt.$$

Note that g is a generalized function if $J \neq \emptyset$ and that g coincides with the inverse Fourier transform of $\mathcal{L}^{(x)}\psi$ up to some constant. Since supp $h_j^{-1} \subset [\xi_{\min}^{(x)}, \xi_{\max}^{(x)}]$ for $j \notin J$ and $c_j \in [\xi_{\min}^{(x)}, \xi_{\max}^{(x)}]$, we may estimate that the support of g (equivalently, the inverse Fourier transform of $\mathcal{L}^{(x)}\psi$) as follows:

$$\operatorname{supp}(g(\xi)) \subset [\xi_{\min}^{(x)}, \xi_{\max}^{(x)}].$$

Summing up the above arguments we arrive at

Lemma 3.2. *Let $\Gamma = \{y : y = a(t), t \in [t_{\min}, t_{\max}]\} \subset \mathbb{R}^3$ be a C^1-smooth curve with $t_{\max} > t_{\min}$. Then*

$$(\mathcal{F}^{-1}\mathcal{L}^{(x)}\psi)(\xi) = \sqrt{2\pi}\left(\sum_{j\notin J} \psi(h_j^{-1}(\xi))\,|(h_j^{-1}(\xi))'| + \sum_{j\in J} \delta(\xi - c_j)\int_{t_{j-1}}^{t_j} \psi(t)\,dt\right). \tag{3.22}$$

Moreover,

$$\operatorname{supp}(\mathcal{F}^{-1}\mathcal{L}^{(x)}\psi) \subset [\xi_{\min}^{(x)}, \xi_{\max}^{(x)}].$$

Below we provide a sufficient condition to ensure trivial intersections of the ranges of two data-to-pattern operators corresponding to different trajectories.

Lemma 3.3. *Let* $\Gamma_a = \{y : y = a(t), t \in [t_{\min}, t_{\max}]\} \subset \mathbb{R}^3$ *and* $\Gamma_b = \{y : y = b(t), t \in [t_{\min}, t_{\max}]\} \subset \mathbb{R}^3$ *be* C^1*-smooth curves such that*

$$\left(\inf_{t\in[t_{\min},t_{\max}]}(t-|x-a(t)|), \sup_{t\in[t_{\min},t_{\max}]}(t-|x-a(t)|)\right) \bigcap \left(\inf_{t\in[t_{\min},t_{\max}]}(t-|x-b(t)|), \sup_{t\in[t_{\min},t_{\max}]}(t-|x-b(t)|)\right) = \emptyset. \tag{3.23}$$

Let $\mathcal{L}_a^{(x)}$ *and* $\mathcal{L}_b^{(x)}$ *be the data-to-pattern operators associated with* Γ_a *and* Γ_b*, respectively. Then* $Range(\mathcal{L}_a^{(x)}) \cap Range(\mathcal{L}_b^{(x)}) = \{0\}$.

Proof. Let $f_a, f_b \in L^2(t_{\min}, t_{\max})$ be such that $(\mathcal{L}_a^{(x)} f_a)(\tau) = (\mathcal{L}_b^{(x)} f_b)(\tau) \coloneqq Q(\tau, x)$. We need to prove $Q(\cdot, x) \equiv 0$. By the definition of $\mathcal{L}$ (see (2.12)), the function

$$\tau \to Q(\tau, x) = \int_{t_{\min}}^{t_{\max}} e^{-i\tau(t-|x-a(t)|)} f_a(t)\, dt = \int_{t_{\min}}^{t_{\max}} e^{-i\tau(t-|x-b(t)|)} f_b(t)\, dt$$

belongs to $L^2(0, K)$. Since $Q(\tau, x)$ is analytic in $\tau \in \mathbb{R}$, the previous relation is well defined for any $\tau \in \mathbb{R}$. By Definition 3.1, we suppose that $\{t_j\}_{j=1}^{n-1}$ and $\{\tilde{t}_j\}_{j=1}^{m-1}$ are division points of the functions $h_a(t) = t - |x - a(t)|$ and $h_b(t) = t - |x - b(t)|$, respectively. Analogously we define $h_{j,a}(t) := t - |x - a_j(t)|$, $h_{j,b}(t) := t - |x - b_j(t)|$, and $J_a := \{j \in \mathbb{N} : 1 \le j \le n, h'_{j,a}(t) \equiv 0, t \in (t_{j-1}, t_j)\}$, $J_b := \{j \in \mathbb{N} : 1 \le j \le m, h'_{j,b}(t) \equiv 0, t \in (\tilde{t}_{j-1}, \tilde{t}_j)\}$. Denote $h_{j,a}(t) \equiv c_{j,a}$ for $j \in J_a$ and $h_{j,b}(t) \equiv c_{j,b}$ for $j \in J_b$. Using the formula (3.21), the function $Q(\cdot, x)$ can be rewritten as the Fourier transforms:

$$Q(\tau, x) = \int_{\mathbb{R}} e^{-i\tau\xi} g_a(\xi, x)\, d\xi = \int_{\mathbb{R}} e^{-i\tau\xi} g_b(\xi, x)\, d\xi, \tag{3.24}$$

with

$$g_a(\xi, x) = \sum_{j\notin J_a} f_a(h_{j,a}^{-1}(\xi))\, |(h_{j,a}^{-1}(\xi))'| + \sum_{j\in J_a} \delta(\xi - c_{j,a}) \int_{t_{j-1}}^{t_j} f_a(t)\, dt,$$

$$g_b(\xi, x) = \sum_{j\notin J_b} f_b(h_{j,b}^{-1}(\xi))\, |(h_{j,b}^{-1}(\xi))'| + \sum_{j\in J_b} \delta(\xi - c_{j,b}) \int_{\tilde{t}_{j-1}}^{\tilde{t}_j} f_b(t)\, dt.$$

This implies $g_a(\xi, x) = g_b(\xi, x)$ for all $\xi \in R$. On the other hand, the support sets of g_a and g_b satisfy

$$\operatorname{supp} g_a(\cdot, x) \subset \left(\inf_{t\in[t_{\min},t_{\max}]}(t-|x-a(t)|), \sup_{t\in[t_{\min},t_{\max}]}(t-|x-a(t)|)\right),$$

$$\operatorname{supp} g_b(\cdot, x) \subset \left(\inf_{t\in[t_{\min},t_{\max}]}(t-|x-b(t)|), \sup_{t\in[t_{\min},t_{\max}]}(t-|x-b(t)|)\right).$$

Hence, by the condition (3.23) we obtain $g_a(\xi, x) = g_b(\xi, x) \equiv 0$ for all $\xi \in \mathbb{R}$. In view of (3.24), we get $Q(\cdot, x) \equiv 0$. □

For any $y \in \mathbb{R}^3$, define the parameter-dependent test functions $\phi_y^{(x)} \in L^2(0,K)$ by

$$\phi_y^{(x)}(k) = \frac{1}{|t_{\max} - t_{\min}|} \int_{t_{\min}}^{t_{\max}} e^{-ik(t-|x-y|)} dt, \quad k \in (0,K). \tag{3.25}$$

Here we stress that the test function $\phi_y^{(x)}$ depends on both the observation point $x \in S_R$ and the test point $y \in \mathbb{R}^3$. The supporting information of the inverse Fourier transform of the above test function is described as follows.

Lemma 3.4. *We have*

$$[\mathcal{F}^{-1}\phi_y^{(x)}](\tau) = \begin{cases} \sqrt{2\pi}/|t_{\max} - t_{\min}| & \text{if} \quad \tau \in [t_{\min} - |x-y|,\ t_{\max} - |x-y|], \\ 0 & \text{if otherwise.} \end{cases} \tag{3.26}$$

Proof. Let $\tau = t - |x-y|$, we can rewrite the function $\phi_y^{(x)}$ as

$$\phi_y^{(x)}(k) = \int_{\mathbb{R}} e^{-ik\tau} g_y(\tau, x)\, d\tau,$$

where

$$g_y(\tau,x) := \begin{cases} \dfrac{1}{|t_{\max} - t_{\min}|} & \text{if } \tau \in [t_{\min} - |x-y|,\ t_{\max} - |x-y|], \\ 0 & \text{if otherwise.} \end{cases}$$

Therefore, $[\mathcal{F}^{-1}\phi_y^{(x)}](\tau) = \sqrt{2\pi} g_y(\tau, x)$. □

In the following we present a necessary condition imposed on the observation point x and radiating period $T := t_{\max} - t_{\min}$ to ensure that the test function $\phi_y^{(x)}$ lies in the range of the data-to-pattern operator.

Lemma 3.5. *If $\phi_y^{(x)} \in \mathrm{Range}(\mathcal{L}^{(x)})$ for some $y \in \mathbb{R}^3$, we have $\xi_{\max}^{(x)} - \xi_{\min}^{(x)} \geq T$. Here $\xi_{\max}^{(x)}$ and $\xi_{\min}^{(x)}$ are defined by* (3.17).

Proof. If $\phi_y^{(x)} \in \mathrm{Range}(\mathcal{L}^{(x)})$, there exists a function $\psi \in L^2(t_{\min}, t_{\max})$ such that $\phi_y^{(x)} = \mathcal{L}^{(x)}\psi$ in $L^2(0,K)$. Since both $\phi_y^{(x)}$ and $\mathcal{L}^{(x)}\psi$ are analytic functions over $\mathbb{R}$, it holds that $\phi_y^{(x)}(k) = (\mathcal{L}^{(x)}\psi)(k)$ for all $k \in \mathbb{R}$. Then their support sets must be identical, i.e., $\mathrm{supp}(\mathcal{F}^{-1}\phi_y^{(x)}) = \mathrm{supp}(\mathcal{F}^{-1}\mathcal{L}^{(x)}\phi) \subset [\xi_{\min}^{(x)}, \xi_{\max}^{(x)}]$, where we have used Lemma 3.2. Hence, the length of $\mathrm{supp}(\mathcal{F}^{-1}\phi_y^{(x)})$, which can be seen from Lemma 3.4, must be less than or equal to that of $[\xi_{\min}^{(x)}, \xi_{\max}^{(x)}]$, i.e.,

$$\xi_{\max}^{(x)} - \xi_{\min}^{(x)} \geq t_{\max} - t_{\min} = T.$$

□

From the above lemma we conclude that $\phi_y^{(x)} \notin \mathrm{Range}(\mathcal{L}^{(x)})$ for all $y \in \mathbb{R}^3$, if $\xi_{\max}^{(x)} - \xi_{\min}^{(x)} < T$. Inspired by this fact we introduce the concept of observable points.

Definition 3.6. *Let $\xi_{\min}^{(x)}$ and $\xi_{\max}^{(x)}$ be the maximum and minimum of the function $h(t) = t - |x - a(t)| \in C^1[t_{\min}, t_{\max}]$ (see (3.17)), respectively. The point $x \in \mathbb{R}^3$ is called an observable point if $\xi_{\max}^{(x)} - \xi_{\min}^{(x)} \geq T$. The point x is called non-observable if $\xi_{\max}^{(x)} - \xi_{\min}^{(x)} < T$.*

We remark that the set of observable points is uniquely determined by the orbit function $a(t)$ together with the starting and terminal time points $t_{\min}$ and $t_{\max}$. For non-observable points x, one cannot extract information on the orbit function by our approach, which will be explained in the second assertion of Theorem 4.1 below. If x is observable and $\frac{x-a(t)}{|x-a(t)|} \cdot a'(t) \geq 0$ for all $t \in [t_{\min}, t_{\max}]$, the smallest annulus containing the trajectory and centered at x can be recovered. If x is observable but $\frac{x-a(t)}{|x-a(t)|} \cdot a'(t) \geq 0$ for all $t \in [t_{\min}, t_{\max}]$ is not valid, another thinner annulus centered at x can be imaged. Below we derive the observable points for orbit functions given by a straight line (see Fig. 2) and a semi-circle (see Fig. 3) in there dimensions.

Example 1: A straight line segment in $\mathbb{R}^3$.

Suppose that an acoustic point source is moving along a straight line.

Lemma 3.7. *Define the orbit function $a(t) := (0, 0, 2t) \in \mathbb{R}^3$ for $t \in [1, 2]$. Then the point $x = (x_1, x_2, x_3) \in \mathbb{R}^3$, $|x| = 6$ is observable if $x_3 \in [-6, \frac{3-\sqrt{33}}{2}] \bigcup [3, 6]$.*

Proof. From the expression of the orbit function $a(t)$, we have

$$h(t) = t - |x - a(t)| = t - \sqrt{x_1^2 + x_2^2 + (x_3 - 2t)^2} = t - \sqrt{(2t - x_3)^2 + 36 - x_3^2},$$
$$h'(t) = 1 - |x - a(t)|' = 1 - \frac{2(2t - x_3)}{\sqrt{(2t - x_3)^2 + 36 - x_3^2}}.$$

We notice that $h'(t) \geq 0$ as $t \leq t_0$ and $h'(t) < 0$ as $t > t_0$, where $t_0 := \frac{x_3}{2} + \sqrt{3 - \frac{x_3^2}{12}}$. Hence, there are three cases for the relationship between t_0 and $[1, 2]$.

Case (i): If $t_0 \leq 1$, then $x_3 - 2 \leq -\sqrt{12 - \frac{x_3^2}{3}}$, which means $x_3 \in [-6, \frac{3-\sqrt{33}}{2}]$. In this case, $h(t)$ is monotonically decreasing in $[1, 2]$. So, if x is observable, we have

$$h(1) - h(2) \geq 1,$$

that is,

$$\sqrt{13 - 2x_3} \geq \sqrt{10 - x_3}.$$

Thus, $x \in S_6$ is an observable point if $x_3 \in [-6, \frac{3-\sqrt{33}}{2}]$.

Case (ii): If $t_0 \in [1, 2]$, then $2 - x_3 \leq \sqrt{12 - \frac{x_3^2}{3}} \leq 4 - x_3$, which means $x_3 \in [\frac{3-\sqrt{33}}{2}, 3 - \sqrt{6}]$. In this case, $h(t)$ is monotonically increasing in $[1, t_0]$ and monotonically decreasing in $[t_0, 2]$. We notice that

$$h(t_0) - \min\{h(1), h(2)\} < 1,$$

for all $x_3 \in [\frac{3-\sqrt{33}}{2}, 3 - \sqrt{6}]$.

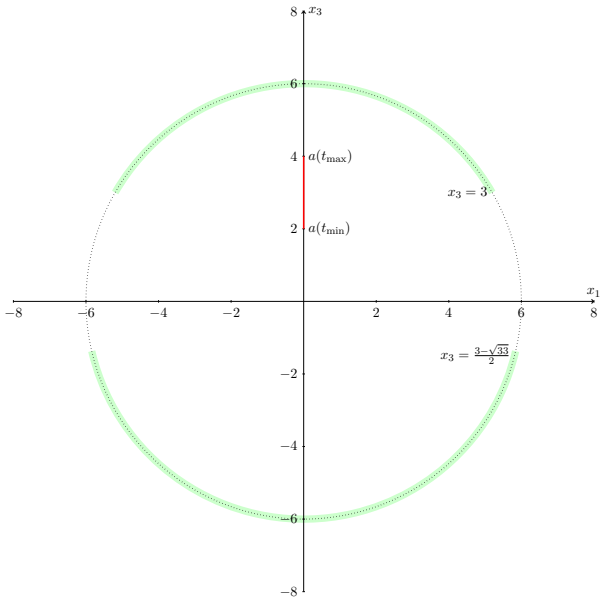

Figure 2: Illustration of observable (green arc) and non-observable (dotted arc) points for the trajectory $a(t) = (0, 0, 2t)$ for $t \in [1, 2]$ in the xOz plane.

Case (iii): If $t_0 \geq 2$, then $x_3 - 4 \leq -\sqrt{12 - \frac{x_3^2}{3}}$, which means $x_3 \in [3 - \sqrt{6}, 6]$. In this case, $h(t)$ is monotonically increasing in $[1, 2]$. So, if x is observable, we have

$$h(2) - h(1) \geq 1,$$

that is,

$$\sqrt{13 - 2x_3} \leq \sqrt{10 - x_3}.$$

Thus, $x \in S_6$ is an observable point if $x_3 \in [3, 6]$.

To sum up, we deduce that an observable point $x \in \mathbb{R}^3, |x| = 6$ should fulfill the relation

$$x_3 \in [-6, \frac{3 - \sqrt{33}}{2}] \bigcup [3, 6].$$

□

Example 2: A semi-circle in $\mathbb{R}^3$.

Suppose that an acoustic point source is moving along the semi-circle centered at $z = (z_1, z_2, z_3) \in \mathbb{R}^3$.

Lemma 3.8. *Let the orbit function be $a(t) = (0.5 \cos t + z_1, 0.5 \sin t + z_2, z_3) \in \mathbb{R}^3$ for $t \in [\pi, 2\pi]$. Then $x = (x_1, x_2, x_3) \notin \Gamma$ is observable if $x_1 \geq z_1$.*

Proof. From the orbit function $a(t)$, we have

$$h(t) = t - |x - a(t)| = t - \sqrt{(x_1 - z_1 - 0.5\cos t)^2 + (x_2 - z_2 - 0.5\sin t)^2 + (x_3 - z_3)^2}.$$

It is obvious that $|a'(t)| < 1$ and then get $h'(t) > 0$ for all $t \in [\pi, 2\pi]$. That means the function $h(t)$ is monotonically increasing in $[\pi, 2\pi]$. So, there is

$$\begin{aligned} \xi^{(x)}_{\min} &= \pi - \sqrt{(x_1 - z_1 + 0.5)^2 + (x_2 - z_2)^2 + (x_3 - z_3)^2}, \\ \xi^{(x)}_{\max} &= 2\pi - \sqrt{(x_1 - z_1 - 0.5)^2 + (x_2 - z_2)^2 + (x_3 - z_3)^2}. \end{aligned}$$

If x is observable, we have

$$\begin{aligned} \xi^{(x)}_{\max} - \xi^{(x)}_{\min} &= \pi - \sqrt{(x_1 - z_1 - 0.5)^2 + (x_2 - z_2)^2 + (x_3 - z_3)^2} \\ &\quad + \sqrt{(x_1 - z_1 + 0.5)^2 + (x_2 - z_2)^2 + (x_3 - z_3)^2} \\ &\geq T = \pi, \end{aligned}$$

that is,

$$(x_1 - (z_1 - 0.5))^2 \geq (x_1 - (z_1 + 0.5))^2.$$

One can find $x_1 \geq z_1$ through simple calculations. □

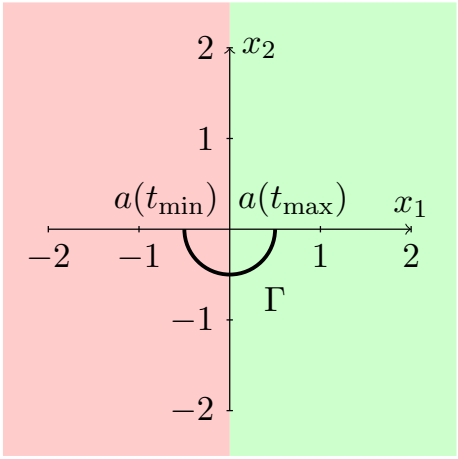

Figure 3: Illustration of the observable (green area removes the portion that intersects trajectory Γ) and non-observable (red area) points for the trajectory $a(t) = (0.5\cos t, 0.5\sin t, 0)$ with $t \in [\pi, 2\pi]$ in the xOy plane.

Given the trajectory $\Gamma = \{y : y = a(t),\, t \in [t_{\min}, t_{\max}]\}$, the set

$$\Lambda_\Gamma := \{y \in \mathbb{R}^3 : \inf_{z\in\Gamma} |x - z| \le |x - y| \le \sup_{z\in\Gamma} |x - z|\}$$

denotes the smallest annulus containing Γ and centered at the point x. One can at most expect to recover this annulus from the multi-frequency data taken at a single observation point. If x is an observable point, we define the annulus (see Fig. 4)

$$A_\Gamma^{(x)} := \{y \in \mathbb{R}^3 : t_{\max} - \xi_{\max}^{(x)} \le |x - y| \le t_{\min} - \xi_{\min}^{(x)}\} \subset \mathbb{R}^3. \tag{3.27}$$

Remark 3.9. *If the point source keeps stationary at $z \in \mathbb{R}^3$, that is, $\Gamma = \{z\}$, then each point $x \in \mathbb{R}^3\backslash\{z\}$ is observable. In this case, the annulus $A_\Gamma^{(x)}$ degenerates into a ring. It can be said that the concept of non-observable points is produced by the movement of the point source.*

If $h'(t) > 0$ for $t \in (t_{\min}, t_{\max})$, we have

$$A_\Gamma^{(x)} = \{y \in \mathbb{R}^3 : |x - a(t_{\max})| \le |x - y| \le |x - a(t_{\min})|\}$$

which is a subset of Λ_Γ and coincides with Λ_Γ when $\frac{x-a(t)}{|x-a(t)|} \cdot a'(t) > 0$ for all $t \in [t_{\min}, t_{\max}]$;

If $h'(t) < 0$ for $t \in (t_{\min}, t_{\max})$, there holds

$$A_\Gamma^{(x)} = \{y \in \mathbb{R}^3 : |x - a(t_{\min})| + T \le |x - y| \le |x - a(t_{\max})| - T\},$$

which is also a subset of Λ_Γ; see Lemma 3.10 below.

Lemma 3.10. *Let $x \in S_R$ be an observable point. We have*

$$\inf_{z\in\Gamma} |x - z| \le |x - y| \le \sup_{z\in\Gamma} |x - z| \quad \textit{for all} \quad y \in A_\Gamma^{(x)}.$$

Proof. Suppose that

$$\xi_{\min}^{(x)} = t_1 - |x - a(t_1)|, \quad \xi_{\max}^{(x)} = t_2 - |x - a(t_2)|, \quad \text{for some} \quad t_1, t_2 \in [t_{\min}, t_{\max}].$$

Therefore,

$$\begin{aligned} t_{\min} - \xi_{\min}^{(x)} &= t_{\min} - t_1 + |x - a(t_1)| \le |x - a(t_1)| \le \sup_{z\in\Gamma} |x - z|, \\ t_{\max} - \xi_{\max}^{(x)} &= t_{\max} - t_2 + |x - a(t_2)| \ge |x - a(t_2)| \ge \inf_{z\in\Gamma} |x - z|. \end{aligned}$$

This implies that for $y \in A_\Gamma^{(x)}$,

$$|x - y| \ge t_{\max} - \xi_{\max}^{(x)} \ge \inf_{z\in\Gamma} |x - z|, \quad |x - y| \le t_{\min} - \xi_{\min}^{(x)} \le \sup_{z\in\Gamma} |x - z|.$$

□

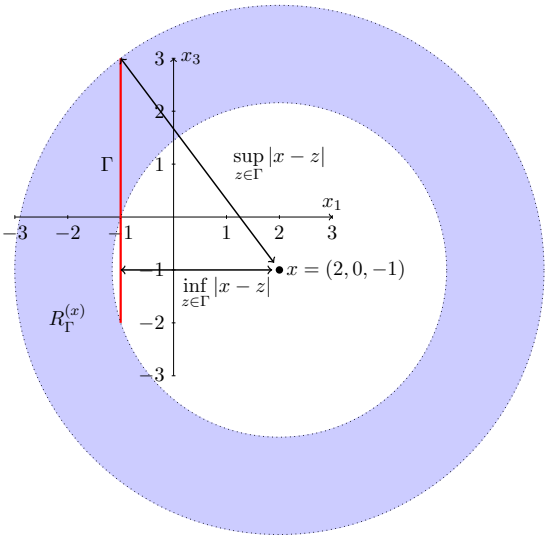

Figure 4: Illustration of the annulus $A_\Gamma^{(x)}$ (blue area) with $x = (2, 0, 1)$ in the xOz plane. Here the curve $a(t) = (-1, 0, 4-t)$, $t \in [1, 6]$ denotes the orbit (the red segment) of a point source moving from below to above. There holds $|x-a(t_{\max})| = \sqrt{10}$, $|x-a(t_{\min})| = 5$, $\inf\limits_{z\in\Gamma}|x-z| = 3$, $\sup\limits_{z\in\Gamma}|x-z| = 5$. In this case the annulus $A_\Gamma^{(x)}$ is a subset of $\{y \in \mathbb{R}^3 : \inf\limits_{z\in\Gamma}|x-z| \le |x-y| \le \sup\limits_{z\in\Gamma}|x-z|\}$.

If $x \in S_R$ is observable, we shall prove that the test function $\phi_y^{(x)}$ lies in the range of $\mathcal{L}^{(x)}$ if and only if $y \in A_\Gamma^{(x)}$. This together with (2.15) establishes a computational criterion for imaging $A_\Gamma^{(x)}$ from the multi-frequency near-field data $u(x, k)$ with $k \in [k_{\min}, k_{\max}]$. We also need to discuss non-observable points.

Lemma 3.11. *(i) If x is non-observable, we have $\phi_y^{(x)} \notin \mathrm{Range}(\mathcal{L}^{(x)})$ for all $y \in \mathbb{R}^3$.*
(ii) If x is an observable point, we have $\phi_y^{(x)} \in \mathrm{Range}(\mathcal{L}^{(x)})$ if and only if $y \in A_\Gamma^{(x)}$.

Proof. (i) The first assertion follows directly from Lemma 3.5 and the Definition 3.6 for non-observable points.

(ii) If x is an observable point, we have $\xi_{\max}^{(x)} - \xi_{\min}^{(x)} \ge T$. If $\phi_y^{(x)} \in \mathrm{Range}(\mathcal{L}^{(x)})$, one can find a function ϕ satisfying $\phi_y^{(x)} = \mathcal{L}^{(x)}\phi$. Then their support sets must fulfill the relation $\mathrm{supp}(\mathcal{F}^{-1}\phi_y^{(x)}) = \mathrm{supp}(\mathcal{F}^{-1}\mathcal{L}^{(x)}\phi) \subset [\xi_{\min}^{(x)}, \xi_{\max}^{(x)}]$ by Lemma 3.3. Using Lemma 3.4 yields

$$[t_{\min} - |x-y|, t_{\max} - |x-y|] \subset [\xi_{\min}^{(x)}, \xi_{\max}^{(x)}].$$

Hence, $t_{\min} - |x-y| \ge \xi_{\min}^{(x)}$ and $t_{\max} - |x-y| \le \xi_{\max}^{(x)}$, leading to

$$t_{\max} - \xi_{\max}^{(x)} \le |x-y| \le t_{\min} - \xi_{\min}^{(x)}.$$

This proves $y \in A_\Gamma^{(x)}$.

On the other hand, if $y \in A_\Gamma^{(x)}$, we have

$$[t_{\min} - |x-y|, t_{\max} - |x-y|] \subset [\xi_{\min}^{(x)}, \xi_{\max}^{(x)}].$$

Setting

$$\psi(t) := \frac{e^{ik(|x-a(t)|-|x-y|)}}{T} \in L^2(t_{\min}, t_{\max}),$$

we find $\phi_y^{(x)}(k) = (\mathcal{L}^{(x)}\psi)(k)$. Therefore, $\phi_y^{(x)}(k) \in$ Range$(\mathcal{L}^{(x)})$.

□

4 Indicator functions and uniqueness

If x is an observable point, we know from Lemma 3.11 that the test functions $\phi_y^{(x)}$ can be utilized to characterize $A_\Gamma^{(x)}$ through (2.15). Hence, we define the indicator function

$$W^{(x)}(y) := \left[\sum_{n=1}^{\infty} \frac{|\langle \phi_y^{(x)}, \psi_n^{(x)} \rangle|^2_{L^2(0,K)}}{|\lambda_n^{(x)}|}\right]^{-1}, \qquad y \in \mathbb{R}^3. \tag{4.28}$$

Combining Theorem 2.4, Lemma 3.11 and Picard theorem, we obtain

Theorem 4.1. *If x is an observable point, it holds that*

$$W^{(x)}(y) = \begin{cases} 0 & \text{if} \quad y \notin A_\Gamma^{(x)}, \\ \text{finite positive number} & \text{if} \quad y \in A_\Gamma^{(x)}. \end{cases}$$

If x is non-observable, we have $W^{(x)}(y) = 0$ for all $y \in \mathbb{R}^3$.

Hence, for observable points the values of $W^{(x)}$ in the annulus $A_\Gamma^{(x)}$ should be relatively bigger than those elsewhere. The values of $W^{(x)}$ vanished identically in $\mathbb{R}^3$ if x is non-observable.

Remark 4.2. *The trajectory Γ can not be uniquely determined by one observable point x. For example, let $\Gamma_1 = \{z_1\}$ and $\Gamma_2 = \{z_2\}$ be given by two stationary points such that*

$$z_1 \neq z_2, \ |x - z_1| = |x - z_2|.$$

Then, by the definition (4.28) of $W^{(x)}$, we have $A_{\Gamma_1}^{(x)} = A_{\Gamma_2}^{(x)} = \{y \in \mathbb{R}^3 : |x-y| = |x-z_j|, j = 1, 2\}$.

In the case of sparse observable points $\{x_j \in S_R : j = 1, 2, \cdots, M\}$, we shall make use of the following indicator function:

$$W(y) = \left[\sum_{j=1}^{M} \frac{1}{W^{(x_j)}(y)}\right]^{-1} = \left[\sum_{j=1}^{M}\sum_{n=1}^{\infty} \frac{|\langle \phi_y^{(x_j)}, \psi_n^{(x_j)} \rangle|^2_{L^2(0,K)}}{|\lambda_n^{(x_j)}|}\right]^{-1}, \qquad y \in \mathbb{R}^3. \tag{4.29}$$

Define the domain D_Γ associated with the observable points $\{x_j : j = 1, 2, \cdots, M\}$ as

$$D_\Gamma := \bigcap_{j=1,2,\cdots,M} A_\Gamma^{(x_j)}. \tag{4.30}$$

We can reconstruct D_Γ from the multi-frequency near-field data measured at sparse observable points.

Theorem 4.3. *It holds that $0 < W(y) < +\infty$ if $y \in D_\Gamma$ and $W(y) = 0$ if $y \notin D_\Gamma$.*

Proof. If $y \in D_\Gamma$, it means that $y \in A_\Gamma^{(x_j)}$ for $j = 1, 2, \cdots, M$. By Theorem 4.1,

$$\sum_{n=1}^{\infty} \frac{|\langle \phi_y^{(x_j)}, \psi_n^{(x_j)} \rangle|^2_{L^2(0,K)}}{|\lambda_n^{(x_j)}|} < +\infty \quad \text{for all} \quad j = 1, 2, \cdots, M. \tag{4.31}$$

Then the finite sum over the index j must fulfill the relation $0 < W(y) < +\infty$.

If $y \notin D_\Gamma$, we may suppose without loss of generality that $y \notin A_\Gamma^{(x_1)}$. By Theorem 4.1,

$$[W^{(x_1)}(y)]^{-1} = \sum_{n=1}^{\infty} \frac{|\langle \phi_y^{(x_1)}, \psi_n^{(x_1)} \rangle|^2_{L^2(0,K)}}{|\lambda_n^{(x_1)}|} = \infty.$$

Together with the definition of W, this gives

$$W(y) < \left[\sum_{n=1}^{\infty} \frac{|\langle \phi_y^{(x_1)}, \psi_n^{(x_1)} \rangle|^2_{L^2(0,K)}}{|\lambda_n^{(x_1)}|} \right]^{-1} = 0.$$

□

Consequently, we arrive at the following uniqueness results, which seem unknown in the literature.

Theorem 4.4. *Denote by $\Gamma = \{a(t) : t \in [t_{\min}, t_{\max}]\}$ the trajectory of a moving point source where $a \in C^1[t_{\min}, t_{\max}]$.*

(i) The domain D_Γ associated with all observable points $x \in S_R$ (see (4.30)) can be uniquely determined by the multi-frequency data $\{u(x, k) : x \in S_R, k \in (k_{\min}, k_{\max})\}$.

(ii) Let $x \in S_R$ be an arbitrarily fixed observable point. Then the annulus $A_\Gamma^{(x)}$ (see (3.27)) can be uniquely determined by the multi-frequency data $\{u(x, k) : k \in (k_{\min}, k_{\max})\}$. In particular, the annulus Λ_Γ can be uniquely recovered if $\frac{x-a(t)}{|x-a(t)|} \cdot a'(t) > 0$ in $[t_{\min}, t_{\max}]$.

Remark 4.5. *Physically, the condition $\frac{x-a(t)}{|x-a(t)|} \cdot a'(t) > 0$ in the second assertion of Theorem 4.4 means that the function $h(t) = t - |x - a(t)|$ is monotonically increasing and the function $|x - a(t)|$ is monotonically decreasing in $[t_{\min}, t_{\max}]$.*

The second assertion of Theorem 4.4 answers the question what kind of information can be extracted from the multi-frequency data measured at a single observable point. Unfortunately, we do not know whether an observation point is observable or not, if there is no a priori information on the orbit function.

5 Numerical implements

In this section, we conducted a couple of numerical experiments to validate our algorithm in three dimensions. In practice, the time-domain data is usually Fourier transformed to the multi-frequency data. However, to simplify the numerical procedures for simulation, we carried out computational tests only in the frequency domain. Our goal is to extract information on the trajectory of a moving point source from multi-frequency near-field data that were taken at one or sparce observation points.

Assuming a wave-number-dependent source term$f(x,k)$, as defined in (1.5), we can synthesize the near-field pattern using equation (1.9)

$$w(x,k)=\frac{1}{\sqrt{32\pi^3}}\int_{t_{\min}}^{t_{\max}}\frac{e^{-ik(t-|x-a(t)|)}}{|x-a(t)|}g(t)\,dt,\quad x\in S_R\,,\ k\in(k_{\min},k_{\max}),\tag{5.32}$$

where $S_R=\{x\in\mathbb{R}^3:\,|x|=R\}$. The signal strength function $g(t)$ is defined as $g(t)=(t+1)^2$ fulfilling the coercivity constraint in our numerical examples below. Now we will introduce the process of the inversion algorithm. The frequency interval $(0,K)$ can be discretized by defining

$$k_n=(n-0.5)\Delta k,\quad \Delta k:=\frac{K}{N},\quad n=1,2,\cdots,N.$$

To approximate the integral in (2.10), we adopt $2N-1$ samples $w(x,\kappa+k_n),n=1,2,\cdots,N$ and $w(x,\kappa-k_n),n=1,2,\cdots,N-1$, of the near field and apply the midpoint rule. Therefore, we have

$$(\mathcal{N}^{(x)}\phi)(\tau_n)\approx\sum_{m=1}^{N}w(x,\kappa+\tau_n-s_m)\phi(s_m)\Delta k,\tag{5.33}$$

where $\tau_n:=n\Delta k$ and $s_m:=(m-0.5)\Delta k$, $n,m=1,2,\cdots,N$. The Toeplitz matrix provides a discrete approximation of the near field operator $\mathcal{N}^{(x)}$:

$$\mathcal{N}^{(x)}:=\Delta k\begin{pmatrix} w(\hat{x},\kappa+k_1) & w(\hat{x},\kappa-k_1) & \cdots & w(\hat{x},\kappa-k_{N-2}) & w(\hat{x},\kappa-k_{N-1})\\ w(\hat{x},\kappa+k_2) & w(\hat{x},\kappa+k_1) & \cdots & w(\hat{x},\kappa-k_{N-3}) & w(\hat{x},\kappa-k_{N-2})\\ \vdots & \vdots & & \vdots & \vdots\\ w(\hat{x},\kappa+k_{N-1}) & w(\hat{x},\kappa+k_{N-2}) & \cdots & w(\hat{x},\kappa+k_1) & w(\hat{x},\kappa-k_1)\\ w(\hat{x},\kappa+k_N) & w(\hat{x},\kappa+k_{N-1}) & \cdots & w(\hat{x},\kappa+k_2) & w(\hat{x},\kappa+k_1)\end{pmatrix}\tag{5.34}$$

where $\mathcal{N}^{(x)}$ is a $N\times N$ complex matrix. For any point $y\in\mathbb{R}^3$ we define the test function vector $\phi_y^{(x)}\in\mathbb{C}^N$ from (3.25) by

$$\phi_y^{(x)}:=\left(\frac{1}{t_{max}-t_{min}}\int_{t_{min}}^{t_{max}}e^{-i\tau_1(t-|x-y|)}dt,\,\cdots,\,\frac{1}{t_{max}-t_{min}}\int_{t_{min}}^{t_{max}}e^{-i\tau_N(t-|x-y|)}dt\right).\tag{5.35}$$

Denoting by $\left\{(\tilde{\lambda}_n^{(x)},\psi_n^{(x)}):n=1,2,\cdots,N\right\}$ an eigen-system of the matrix $\mathcal{N}^{(x)}$ (5.34), then one deduces that an eigen-system of the matrix $(\mathcal{N}^{(x)})_{\#}:=|Re(\mathcal{N}^{(x)})|+|Im(\mathcal{N}^{(x)})|$ is

$\left\{(\lambda_n^{(x)}, \psi_n^{(x)}) : n = 1, 2, \cdots, N\right\}$, where $\lambda_n^{(x)} := |Re(\tilde{\lambda}_n^{(x)})| + |Im(\tilde{\lambda}_n^{(\hat{x})})|$. We truncate the indicator function $W^{(x)}$ (4.28) by

$$W^{(x)}(y) := \left[\sum_{n=1}^{N} \frac{\left|\phi_y^{(x)} \cdot \overline{\psi_n^{(x)}}\right|^2}{|\lambda_n^{(x)}|}\right]^{-1}, \quad y \in \mathbb{R}^d, \tag{5.36}$$

where $\cdot$ denotes the inner product in $\mathbb{R}^3$ and N is consistent with the dimension of the Toeplitz matrix (5.34).

The visualization of strip $A_\Gamma^{(x)}$ can be obtained by plotting $W^{(x)}(y)$ and contains information about the source trajectory when an observable point, $x \in S_R$, is considered. This information can be used to image the trajectory of moving point sources represented by straight lines or arcs. The exact trajectory of the moving source is shown using red solid lines in the figures below. We investigate imaging of the moving point sources using near-field data from one or a sparse observation points. In all our numerical examples below, if not otherwise specified, we set $k_{\min} = 0$ for simplicity. The bandwidth can be extended from $(0, k_{max})$ to $(-k_{\max}, k_{\max})$ by $w(x, -k) = \overline{w(x, k)}$. Then, one deduces from these new measurement data with $k_{min} = -k_{max}$ that $\kappa = 0$ and $K = k_{max}$. The frequency band is represented by the interval $(0, 6)$ with $k_{\max} = 6$, $N = 15$ and $\Delta k = 2/5$.

5.1 One observation point

In the following numerical examples of this subsection, the search domain is selected as a cube of the form $[-2, 2] \times [-2, 2] \times [-2, 2]$ and the observation points are chosen from the set $\{x \in \mathbb{R}^3 : |x| = 2\}$. The observation points are then set on a shere with a radius of 2, such that $x = (2\sin\varphi\cos\theta, 2\sin\varphi\sin\theta, 2\cos\varphi)$ for $\theta \in [0, 2\pi]$ and $\varphi \in [0, \pi]$. Figures below illustrate the slices at $y_1 = 0$ or $y_2 = 0$.

Example 1: A straight line segment in $\mathbb{R}^3$

We examine a straight line segment from Example 1, outlined in Section 3. Suppose that the trajectory of the moving point source is give by $a(t) = (0, 0, t - 2)$, where $t \in [1, 3]$ and $x \in S_R = \{x \in \mathbb{R}^3 : |x| = R\}$ represent the observation points. Initially, we must assess the observable and non-observable points. According to the orbit function, we have

$$h(t) = t - |x - a(t)| = t - \sqrt{x_1^2 + x_2^2 + (x_3 - (t-2))^2},$$
$$h'(t) = 1 + \frac{x_3 - (t-2)}{\sqrt{x_1^2 + x_2^2 + (x_3 - (t-2))^2}}.$$

As the second term on the right-hand side of the above equation always falls in the range $[-1, 1]$, it is evident that $h'(t) > 0$ for all $t \in [1, 3]$, indicating that the function $h(t)$ is monotonically

increasing over $[1,3]$ Consequently, $\xi_{min}^{(x)} = h(1)$ and $\xi_{max}^{(x)} = h(3)$ as described in (3.17). We know that the points satisfying $h(3) - h(1) \geq 3 - 1$ are all observable points as illustrated in Definition 3.6. By simple calculations similar to the proof of Lemma 3.7, $x_3 \geq 0$ can be obtained. Consequently, the observation points $x = (x_1, x_2, x_3) \notin \Gamma$ satisfying $x_3 \geq 0$ are all observable. Further more, if $\frac{x-a(t)}{|x-a(t)|} \cdot a'(t) = \frac{x_3-(t-2)}{|x-a(t)|} \geq 0$, then $x_3 \in [1,2]$. Thus, the smallest annulus $\Lambda_\Gamma^{(x)}$ centered at x and containing the trajectory can be recovered if and only if the observable points x satisfies $1 \leq x_3 \leq 2$. If not, one can only get a slimmer annulus $A_\Gamma^{(x)} \subset \Lambda_\Gamma^{(x)}$. Moreover, all observation points x where $x_3 < 0$ are non-observable. The corresponding numerical results are presented in Figs.5, 6 and 7.

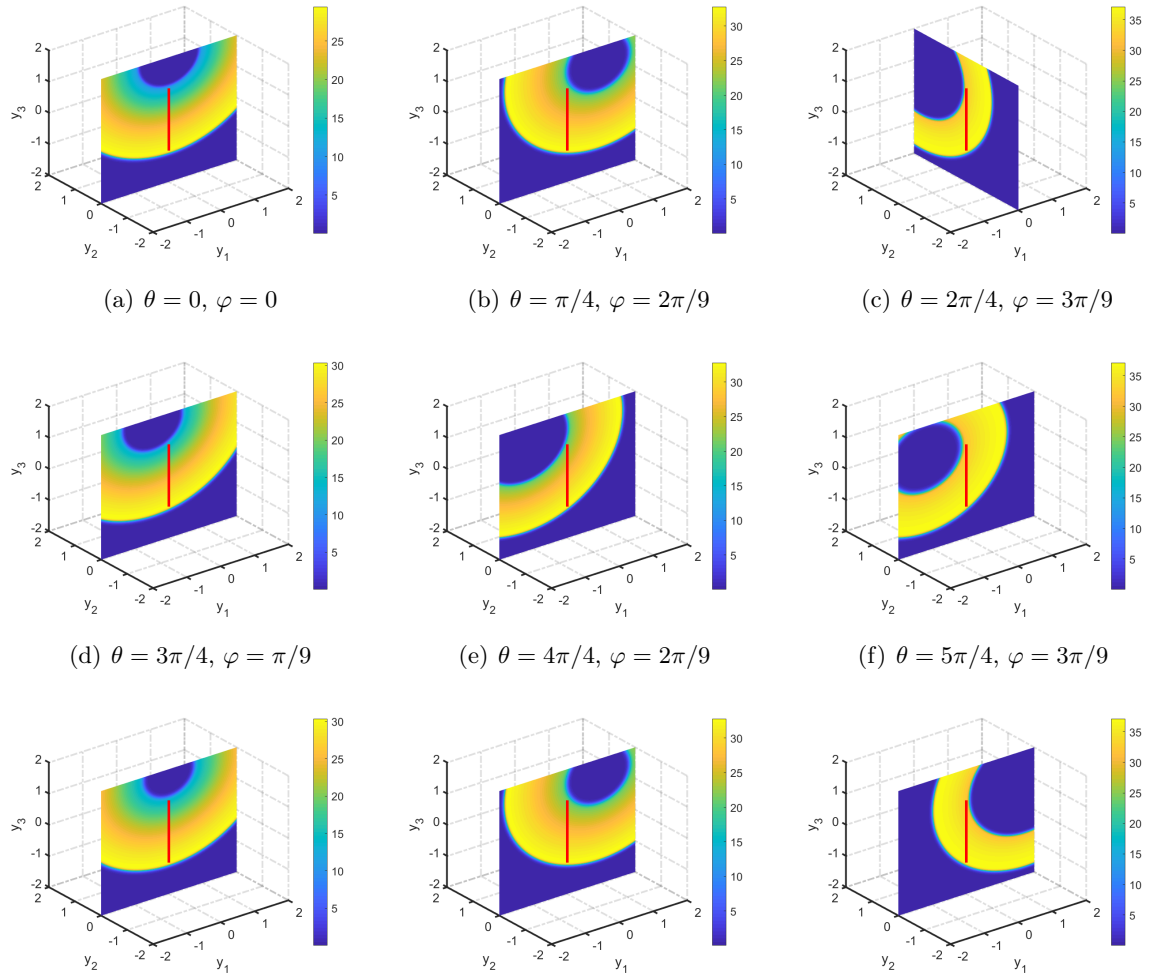

(a) $\theta = 0$, $\varphi = 0$ (b) $\theta = \pi/4$, $\varphi = 2\pi/9$ (c) $\theta = 2\pi/4$, $\varphi = 3\pi/9$

(d) $\theta = 3\pi/4$, $\varphi = \pi/9$ (e) $\theta = 4\pi/4$, $\varphi = 2\pi/9$ (f) $\theta = 5\pi/4$, $\varphi = 3\pi/9$

(g) $\theta = 6\pi/4$, $\varphi = \pi/9$ (h) $\theta = 7\pi/4$, $\varphi = 2\pi/9$ (i) $\theta = 8\pi/4$, $\varphi = 3\pi/9$

Figure 5: Reconstruction from a single observable point $x = (2\sin\varphi\cos\theta, 2\sin\varphi\sin\theta, 2\cos\varphi)$ with $\theta \in [0, 2\pi]$ and $\varphi \in [0, \pi/3]$ for a straight line segment $a(t) = (0, 0, t-2)$ where $t \in [1,3]$. Here it holds that $A_\Gamma^{(x)} = \Lambda_\Gamma^{(x)}$.

In Fig.5, we examine various observable points x, where $\theta \in [0, 2\pi]$ and $\varphi \in [0, \pi/3]$. Specifically, we restrict φ to the range $[0, \pi/3]$, which corresponds to $1 \leq x_3 \leq 2$. We observe that for all $t \in [1, 3]$, $\frac{x-a(t)}{|x-a(t)|} \cdot a'(t) \geq 0$. Consequently, our theoretical predictions ensure that the trajectory of the moving point source can be fully enclosed within the smallest annulus $\Lambda_\Gamma^{(x)}$ centered at x. Notably, our numerical examples demonstrate that $A_\Gamma^{(x)} = \Lambda_\Gamma^{(x)}$.

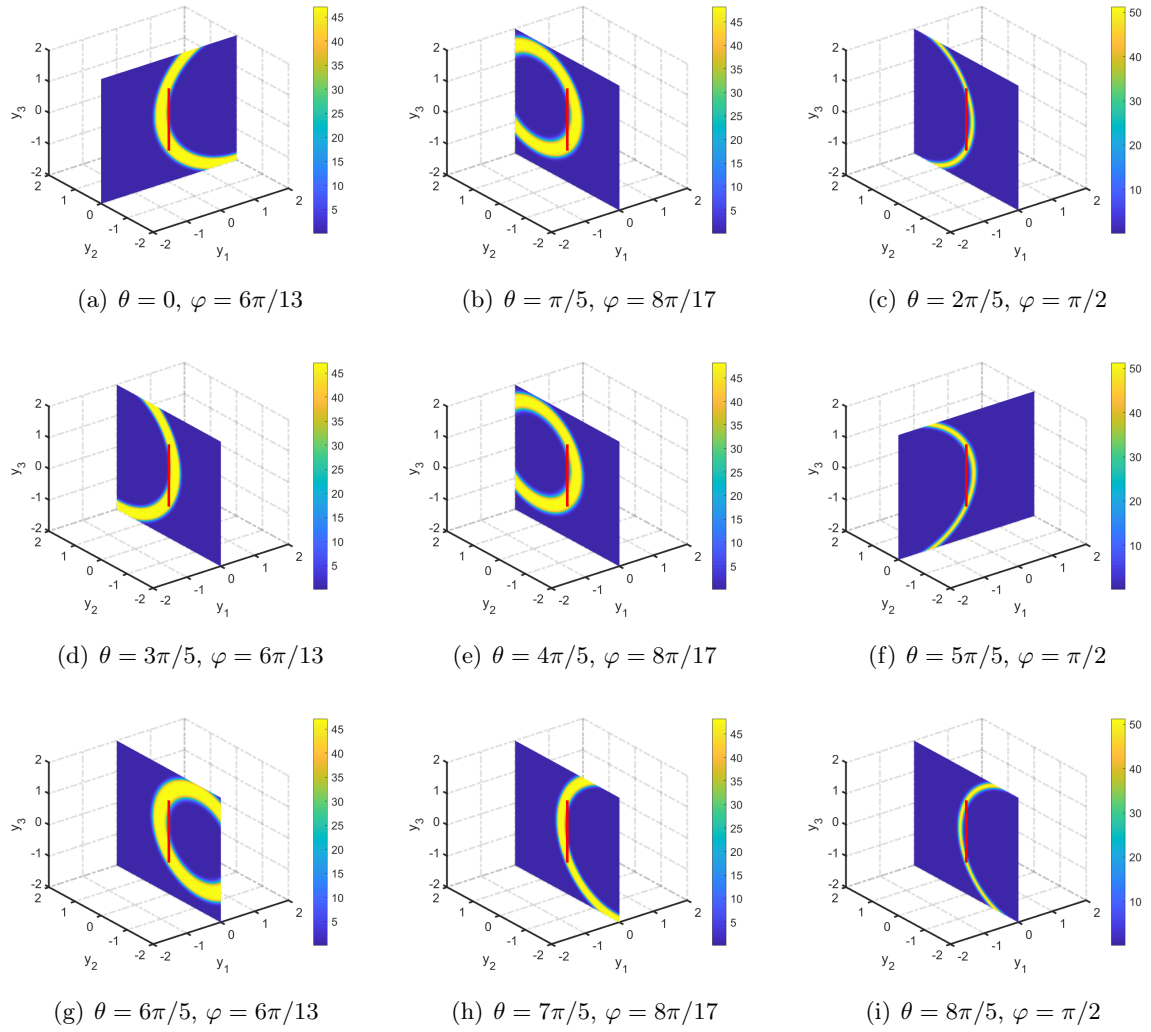

(a) $\theta = 0$, $\varphi = 6\pi/13$ (b) $\theta = \pi/5$, $\varphi = 8\pi/17$ (c) $\theta = 2\pi/5$, $\varphi = \pi/2$

(d) $\theta = 3\pi/5$, $\varphi = 6\pi/13$ (e) $\theta = 4\pi/5$, $\varphi = 8\pi/17$ (f) $\theta = 5\pi/5$, $\varphi = \pi/2$

(g) $\theta = 6\pi/5$, $\varphi = 6\pi/13$ (h) $\theta = 7\pi/5$, $\varphi = 8\pi/17$ (i) $\theta = 8\pi/5$, $\varphi = \pi/2$

Figure 6: Reconstruction from a single observable point $x = (2\sin\varphi\cos\theta, 2\sin\varphi\sin\theta, 2\cos\varphi)$ with $\theta \in [0, 2\pi]$ and $\varphi \in (\pi/3, \pi/2]$ for a straight line segment $a(t) = (0, 0, t-2)$ where $t \in [1, 3]$. Here it holds that $A_\Gamma^{(x)} \subset \Lambda_\Gamma^{(x)}$.

In Fig.6, we collect data at the observable points $x = (2\sin\varphi\cos\theta, 2\sin\varphi\sin\theta, 2\cos\varphi)$ where $\theta \in [0, 2\pi]$ and $\varphi \in (\pi/3, \pi/2]$, such that $0 \leq x_3 < 1$. However, we note that $\frac{x-a(t)}{|x-a(t)|} \cdot a'(t) \geq 0$ no longer holds for all $t \in [1, 3]$. Although these observation points x belong to the observable set, the corresponding annulus $A_\Gamma^{(x)}$ are slimmer than the smallest annulus which encompasses the

trajectory of the moving source and is centered at x. This is because $A_\Gamma^{(x)} \subset \Lambda_\Gamma^{(x)}$, as asserted by Lemma 3.10.

The observation points $x = (2\sin\varphi\cos\theta, 2\sin\varphi\sin\theta,\ 2\cos\varphi)$ are non-observable when $\theta \in [0, 2\pi]$ and $\varphi \in (\pi/2, \pi]$. Numerical results in Fig.7 indicate that the corresponding indicator values are consistently much smaller than 10^{-2}. This is consistent with the outcome of Theorem 4.1, which implies that it is not possible to reconstruct the annulus centered at x which contains partial or whole information on the trajectory of the moving source. The further the non-observable points are from the observable region, the lower the corresponding indicator values. Fig.7 shows that partial information on the trajectory can still be retrieved by our indicator function even at non-observable points, which is an intriguing observation that requires further investigation.

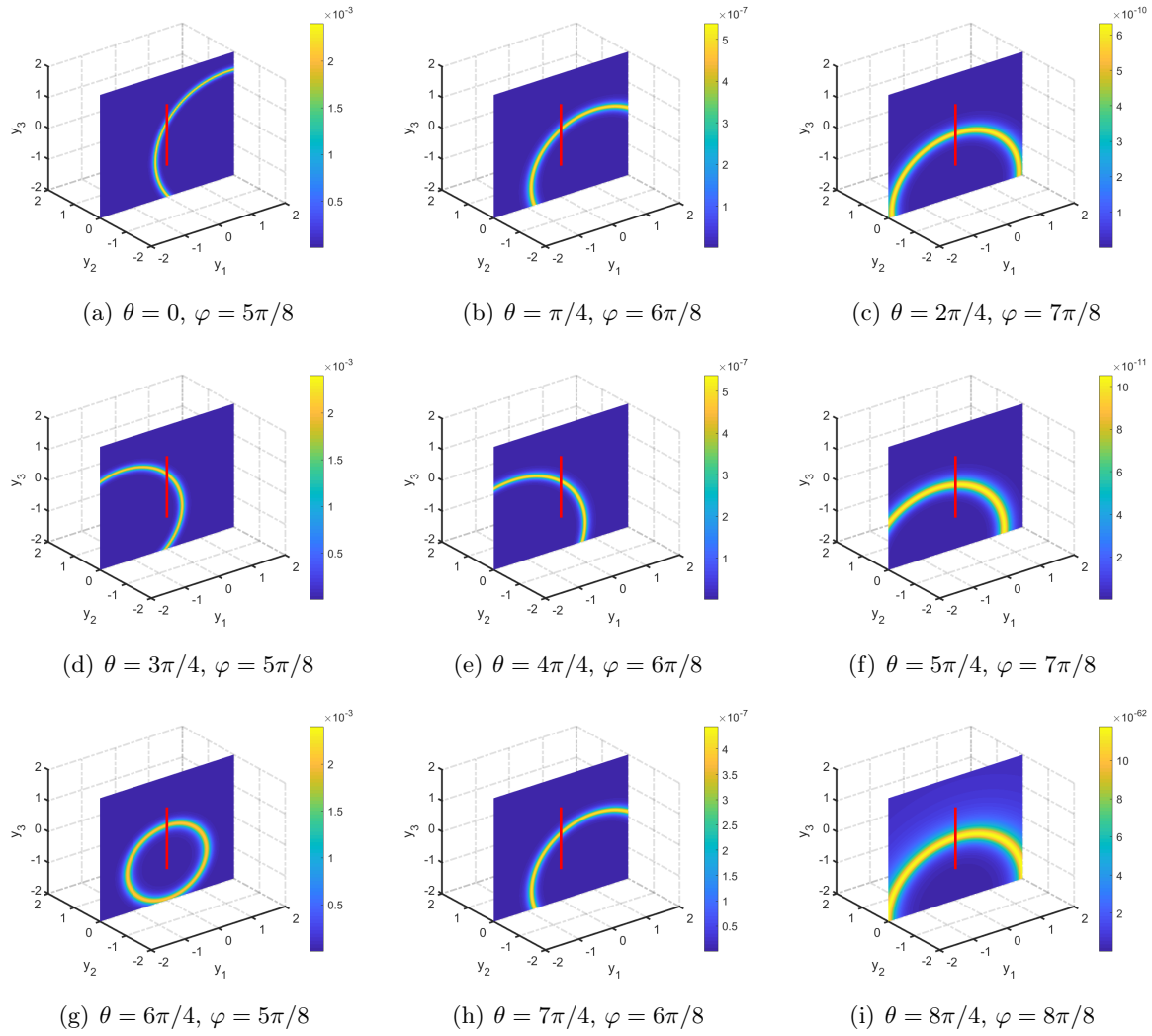

(a) $\theta = 0$, $\varphi = 5\pi/8$ (b) $\theta = \pi/4$, $\varphi = 6\pi/8$ (c) $\theta = 2\pi/4$, $\varphi = 7\pi/8$

(d) $\theta = 3\pi/4$, $\varphi = 5\pi/8$ (e) $\theta = 4\pi/4$, $\varphi = 6\pi/8$ (f) $\theta = 5\pi/4$, $\varphi = 7\pi/8$

(g) $\theta = 6\pi/4$, $\varphi = 5\pi/8$ (h) $\theta = 7\pi/4$, $\varphi = 6\pi/8$ (i) $\theta = 8\pi/4$, $\varphi = 8\pi/8$

Figure 7: Reconstruction from a single non-observable point $x = (2\sin\varphi\cos\theta, 2\sin\varphi\sin\theta, 2\cos\varphi)$ with $\theta \in [0, 2\pi]$ and $\varphi \in (\pi/2, \pi]$ for a straight line segment $a(t) = (0, 0, t-2)$ with $t \in [1, 3]$.

Example 2: An arc in $\mathbb{R}^3$

As demonstrated in Example 2 of Section 3, we consider the trajectory of the moving point given by $a(t) = (0, \cos t, \sin t)$ where $t \in [0, \pi]$. From the orbit function, we obtain

$$h(t) = t - |x - a(t)| = t - \sqrt{x_1^2 + (x_2 - \cos t)^2 + (x_3 - \sin t)^2},$$
$$h'(t) = 1 + \frac{x - a(t)}{|x - a(t)|} \cdot a'(t) = 1 + \frac{-x_2 \sin t + x_3 \cos t}{|x - a(t)|}.$$

It is evident that $|a'(t)| = 1$, thus $h'(t) \geq 0$ for all $t \in [0, \pi]$, which indicates the function $h(t)$ monotonically increases over $[0, \pi]$. Subsequently, we have $\xi_{min}^{(x)} = h(0)$ and $\xi_{max}^{(x)} = h(\pi)$.

According to Definition 3.6, observable points are those that satisfy $h(\pi) - h(0) \geq \pi - 0$. By simple calculations similar to the proof of Lemma 3.8 one can infer that $x_2 \leq 0$. Therefore, the observation points $x = (x_1, x_2, x_3) \notin \Gamma$ that satisfy $x_2 \leq 0$ are all observable. Furthermore, the statement $\frac{x-a(t)}{|x-a(t)|} \cdot a'(t) = \frac{-x_2 \sin t + x_3 \cos t}{|x-a(t)|} \geq 0$ is equivalent to

$$\begin{aligned} -x_2 \sin t + x_3 \cos t &= \sqrt{x_2^2 + x_3^2} \left(\frac{x_3}{\sqrt{x_2^2 + x_3^2}} \sin t - \frac{x_2}{\sqrt{x_2^2 + x_3^2}} \cos t \right) \\ &= \sqrt{x_2^2 + x_3^2} \sin(\alpha - t) \geq 0, \end{aligned}$$

where $\cos \alpha = \frac{x_3}{\sqrt{x_2^2+x_3^2}}$ and $\frac{x_2}{\sqrt{x_2^2+x_3^2}}$. If for all $t \in [0, \pi]$ it holds that $-x_2 \sin t + x_3 \cos t \geq 0$, then it is evident that $\alpha = \pi$, meaning $x_3 = 0$. The smallest annulus $\Lambda_\Gamma^{(x)}$, centered at x and containing the trajectory of the moving source, is recoverable only when the observable points x satisfy $x_3 = 0$. Otherwise, a slimmer annulus $A_\Gamma^{(x)} \subset \Lambda_\Gamma^{(x)}$ can be obtained. Additionally, all observation points x with $x_2 > 0$ are non-observable. The numerical results are presented in Figs.8, 10 and 11.

Fig.8 demonstrates the reconstruction of an arc from observable points $x = (2 \sin \varphi \cos \theta, 2 \sin \varphi \sin \theta, 2 \cos \varphi)$ with $\theta \in [\pi, 2\pi]$ and $\varphi = \pi/2$. We conclude that the trajectory of the moving point source perfectly lies in the smallest annulus centered at x and containing its trajectory. This is due to the selection of observable points x with $x_3 = 0$ and $x_2 \leq 0$, such that $\frac{x-a(t)}{|x-a(t)|} \cdot a'(t) \geq 0$. Here, we have $A_\Gamma^{(x)} = \Lambda_\Gamma$. This effectively demonstrates the effectiveness of our algorithm for imaging an arc in $\mathbb{R}^3$. It is worthy noting that although the arc trajectory of the moving source lies in the annulus depicted in subfigures (a),(b),(c),(g),(h) and (i), they can not be seen clearly since the slice is set at $y_1 = 0$. Therefore, corresponding isosurfaces of the reconstruction are plotted in Fig. 9, showing the trajectory of the moving source perfectly located between the isosurfaces as predicted by our theory.

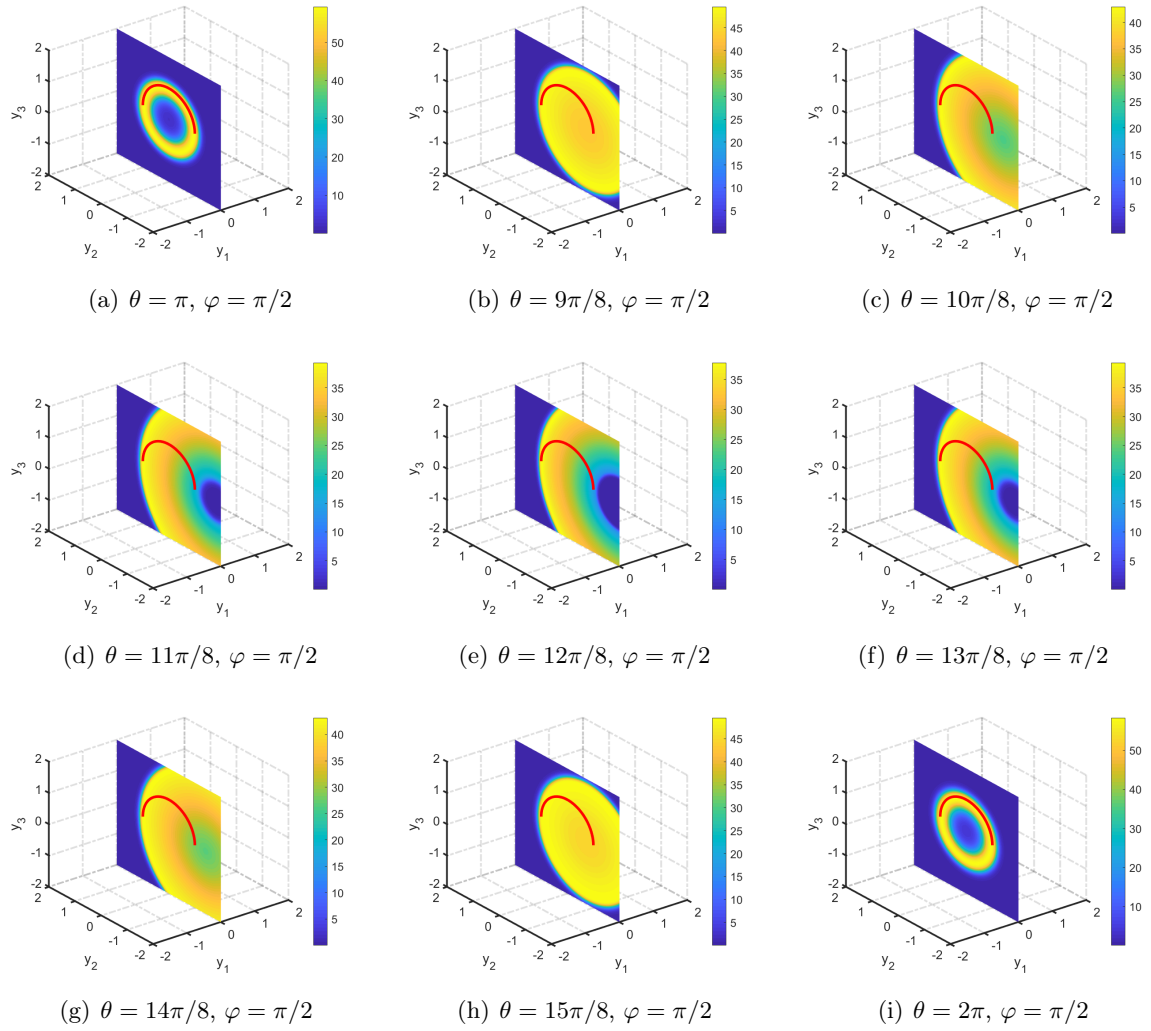

(a) $\theta = \pi$, $\varphi = \pi/2$ (b) $\theta = 9\pi/8$, $\varphi = \pi/2$ (c) $\theta = 10\pi/8$, $\varphi = \pi/2$

(d) $\theta = 11\pi/8$, $\varphi = \pi/2$ (e) $\theta = 12\pi/8$, $\varphi = \pi/2$ (f) $\theta = 13\pi/8$, $\varphi = \pi/2$

(g) $\theta = 14\pi/8$, $\varphi = \pi/2$ (h) $\theta = 15\pi/8$, $\varphi = \pi/2$ (i) $\theta = 2\pi$, $\varphi = \pi/2$

Figure 8: Reconstruction from a single observable point $x = (2\sin\varphi\cos\theta, 2\sin\varphi\sin\theta, 2\cos\varphi)$ with $\theta \in [\pi, 2\pi]$ and $\varphi = \pi/2$ for an arc $a(t) = (0, \cos t, \sin t)$ where $t \in [0, \pi]$. Here it holds that $A_\Gamma^{(x)} = \Lambda_\Gamma^{(x)}$.

Fig.10 displays the reconstructed annulus $A_\Gamma^{(x)}$ which are slimmer than $\Lambda_\Gamma^{(x)}$. This is due to our selection of observable points $x = (2\sin\varphi\cos\theta, 2\sin\varphi\sin\theta, 2\cos\varphi)$ with $\theta \in [\pi, 2\pi]$ and $\varphi = [0, \pi/2) \cup (\pi/2, \pi]$ implying $x_2 \leq 0$ and $x_3 \neq 0$, making it unsuitable to apply $\frac{x-a(t)}{|x-a(t)|} \cdot a'(t) \geq 0$. This results in $A_\Gamma^{(x)} \subset \Lambda_\Gamma^{(x)}$, limiting the retrieval of partial trajectory information. Since $h'(t) > 0$ for $t \in [0, \pi]$, it is possible to capture the starting and end points of the trajectory by $A_\Gamma^{(x)} = \{y \in \mathbb{R}^3 : |x - a(t_{\max})| \leq |x - y| \leq |x - a(t_{\min})|\}$. It should be noted that the size of the annulus depends on the location of the observation points. The numerical results presented in Fig.10 are in agreement with our theory predictions.

Fig.11 presents indicator functions for various non-observable points x =

$(2\sin\varphi\cos\theta, 2\sin\varphi\sin\theta, 2\cos\varphi)$ with $\theta \in (0,\pi)$ and $\varphi \in [0,\pi]$, i.e., $x_2 > 0$. It can be observed that the values of the indicator functions are significantly smaller than 10^{-3}.

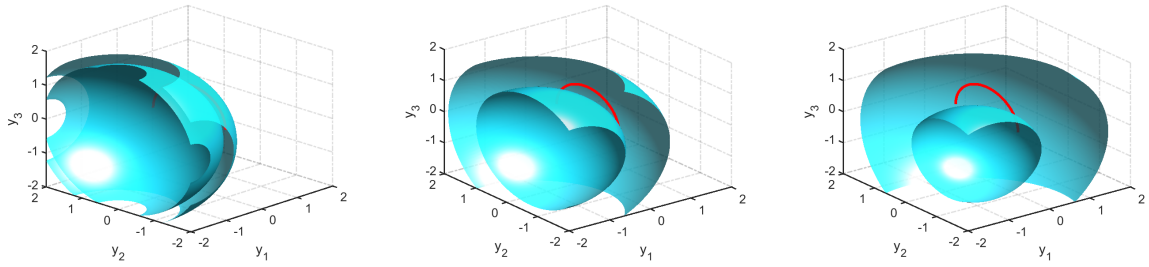

(a) $\theta = \pi$, $\varphi = \pi/2$ (b) $\theta = 9\pi/8$, $\varphi = \pi/2$ (c) $\theta = 10\pi/8$, $\varphi = \pi/2$

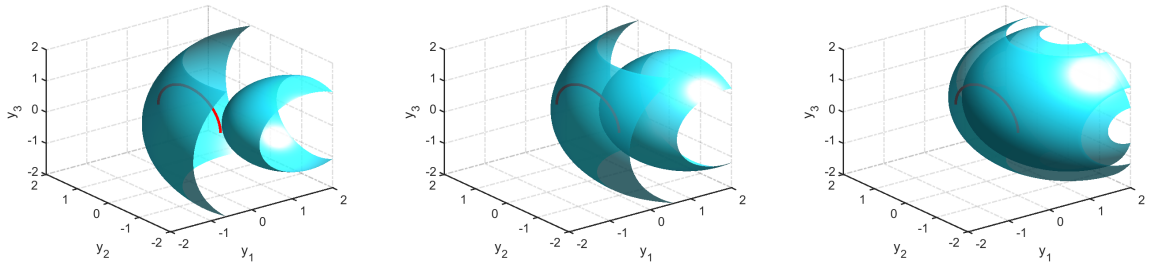

(d) $\theta = 14\pi/8$, $\varphi = \pi/2$ (e) $\theta = 15\pi/8$, $\varphi = \pi/2$ (f) $\theta = 2\pi$, $\varphi = \pi/2$

Figure 9: Iso-surfaces of reconstruction from a single observable point $x = (2\sin\varphi\cos\theta, 2\sin\varphi\sin\theta, 2\cos\varphi)$ with $\theta \in [\pi, 2\pi]$ and $\varphi = \pi/2$ for an arc $a(t) = (0, \cos t, \sin t)$ where $t \in [0,\pi]$. Here it holds that $A_\Gamma^{(x)} = \Lambda_\Gamma^{(x)}$.

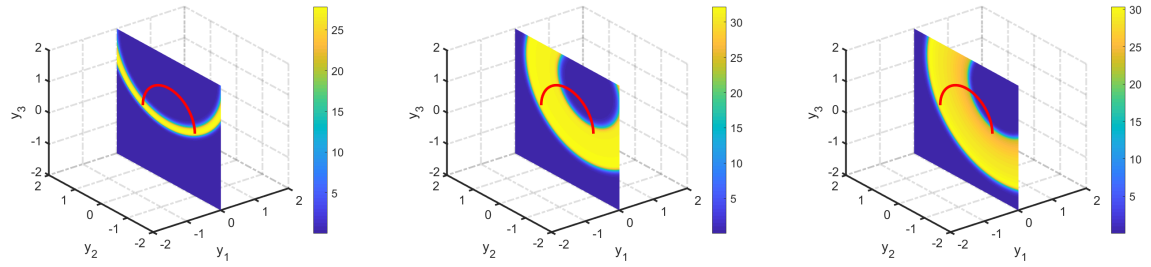

(a) $\theta = \pi$, $\varphi = 0$

(b) $\theta = 6\pi/5$, $\varphi = \pi/4$

(c) $\theta = 7\pi/5$, $\varphi = \pi/4$

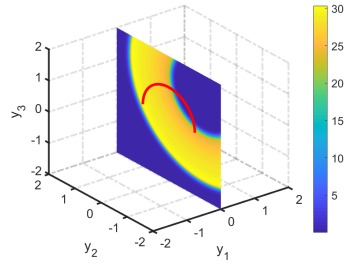

(d) $\theta = 8\pi/5$, $\varphi = \pi/4$

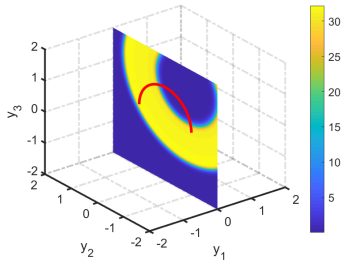

(e) $\theta = 9\pi/5$, $\varphi = \pi/4$

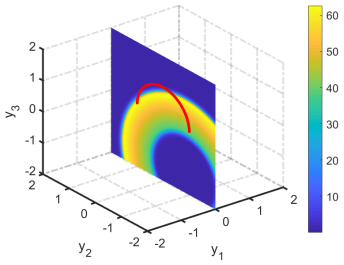

(f) $\theta = 6\pi/5$, $\varphi = 3\pi/4$

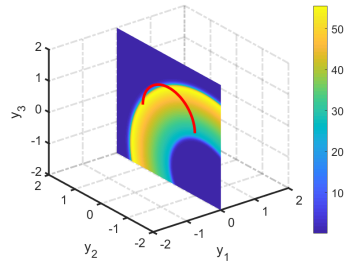

(g) $\theta = 7\pi/5$, $\varphi = 3\pi/4$

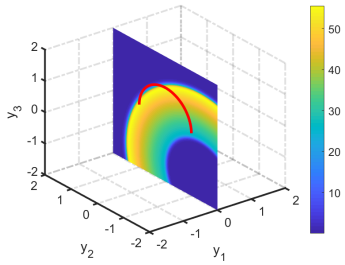

(h) $\theta = 8\pi/5$, $\varphi = 3\pi/4$

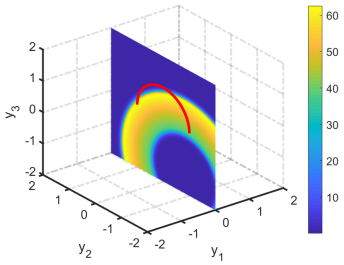

(i) $\theta = 9\pi/5$, $\varphi = 3\pi/4$

Figure 10: Reconstruction from a single observable point $x = (2\sin\varphi\cos\theta, 2\sin\varphi\sin\theta, 2\cos\varphi)$ with $\theta \in [\pi, 2\pi]$ and $\varphi = [0, \pi/2) \cup (\pi/2, \pi]$ for an arc $a(t) = (0, \cos t, \sin t)$ where $t \in [0, \pi]$. Here it holds that $A_\Gamma^{(x)} \subset \Lambda_\Gamma^{(x)}$.

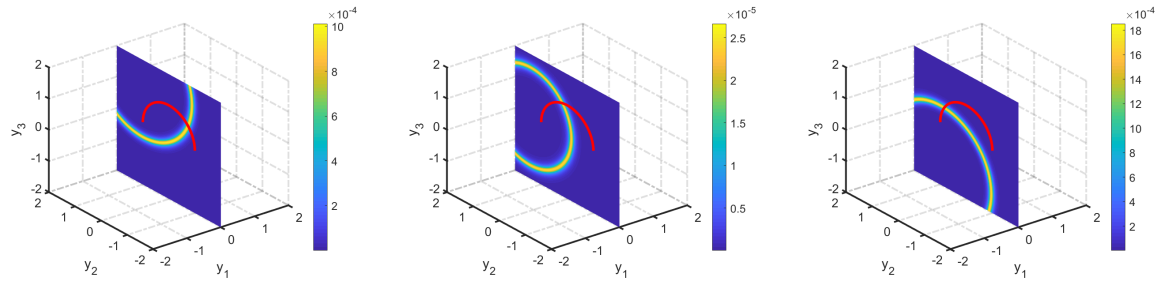

(a) $\theta = \pi/4$, $\varphi = \pi/4$ (b) $\theta = \pi/4$, $\varphi = 2\pi/4$ (c) $\theta = \pi/4$, $\varphi = 3\pi/4$

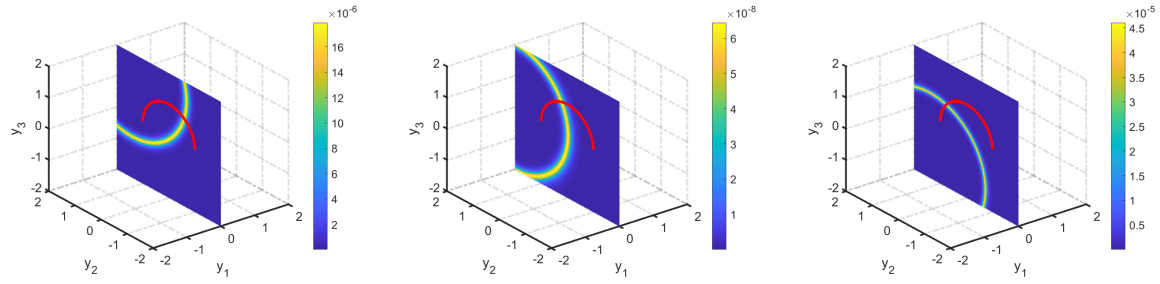

(d) $\theta = 2\pi/4$, $\varphi = \pi/4$ (e) $\theta = 2\pi/4$, $\varphi = 2\pi/4$ (f) $\theta = 2\pi/4$, $\varphi = 3\pi/4$

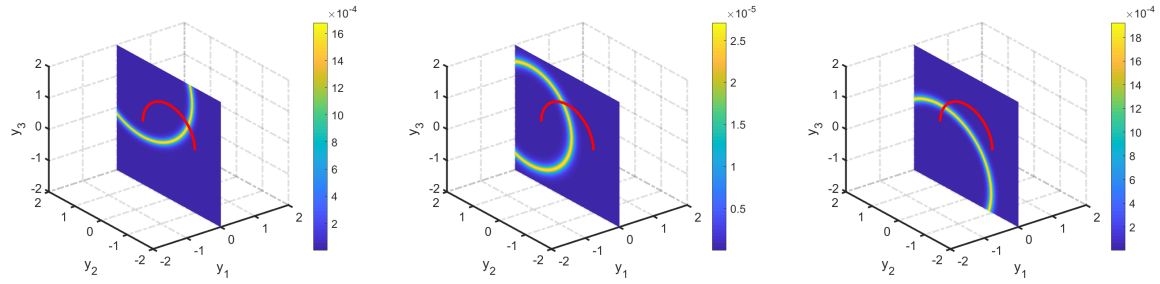

(g) $\theta = 3\pi/4$, $\varphi = \pi/4$ (h) $\theta = 3\pi/4$, $\varphi = 2\pi/4$ (i) $\theta = 3\pi/4$, $\varphi = 3\pi/4$

Figure 11: Reconstruction from a single non-observable point $x = (2\sin\varphi\cos\theta, 2\sin\varphi\sin\theta, 2\cos\varphi)$ with $\theta \in (0,\pi)$ and $\varphi \in [0,\pi]$ for an arc $a(t) = (0, \cos t, \sin t)$ where $t \in [0,\pi]$.

5.2 Sparse observation points

In this subsection, we extend Examples 1 and 2 to include multi-frequency near-field data measured at sparse points. To truncate the indicator function (4.29), we introduce the following expression:

$$W(y) := \left[\sum_{j=1}^{M} \sum_{n=1}^{N} \frac{\left| \phi_y^{(x_j)} \cdot \overline{\psi_n^{(x_j)}} \right|^2}{|\lambda_n^{(x_j)}|} \right]^{-1}, \quad y \in \mathbb{R}^3. \tag{5.37}$$

In this definition, $M > 0$ denotes the number of sparse observation points distributed on S_2. Also, the test function $\phi_y^{(x_j)}$ has the same definition as in (5.35), and $\left\{(\lambda_n^{(x_j)}, \psi_n^{(x_j)}) : n = 1, \cdots, N\right\}$ denotes an eigensystem of the operator $(\mathcal{F}^{(x_j)})_{\#}$. Notably, x_j $(j = 1, 2, \cdots, M)$ may contain both observable and non-observable points. To eliminate the terms similar to

$$\tilde{w}_j = \sum_{n=1}^{N} \frac{\left|\phi_y^{(x_j)} \cdot \overline{\psi_n^{(x_j)}}\right|^2}{|\lambda_n^{(x_j)}|}, \quad j = 1, 2, ...W$$

from the sum in (5.37), we set a threshold $M' > 0$. Precisely, if $\min(\tilde{w}_j(y)) > M'$, the point x_j can be categorized as a non-observable point through the second assertion of Theorem 4.1.

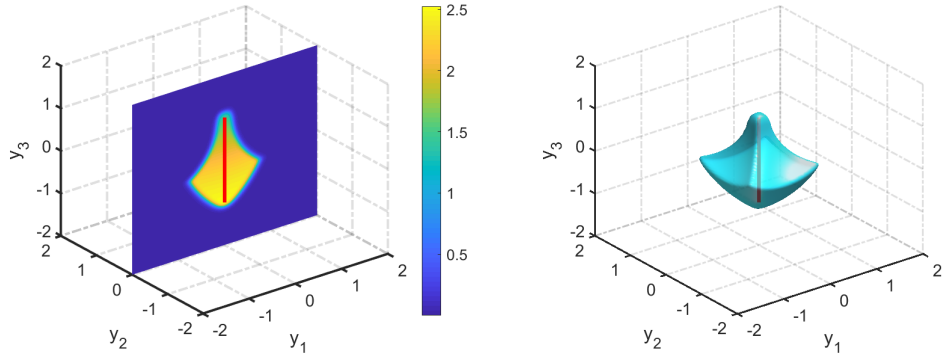

(a) A slice at $y_2 = 0$ (b) Iso-surface level = 2

Figure 12: Reconstruction from sparse observation points $x = (2\sin\varphi\cos\theta, 2\sin\varphi\sin\theta, 2\cos\varphi)$ with $\theta \in [0, 2\pi)$ and $\varphi \in [0, \pi/3]$ for a straight line segment $a(t) = (0, 0, t - 2)$ where $t \in [1, 3]$. Here $M = 13$ denotes the number of the observation points and we take $\theta = (j-1)\pi/2$, $j = 1, \cdots, 4$ and $\varphi = (j-1)\pi/9$, $j = 1, \cdots, 3$ such that $A_\Gamma^{(x_j)} = \Lambda_\Gamma^{(x_j)}$.

Firstly, assuming that all the selected observation points are observable, and that the angle between the vector connecting these observable points and the trajectory points, and the velocity vector of the moving point source, lies within the range of $[0, \pi/2]$, implying $\frac{x-a(t)}{|x-a(t)|} \cdot a'(t) \geq 0$. For every observation point, it is possible to extract the smallest annulus centered at the observation point and containing the trajectory of the moving point source. In Figs.12 and 13, we use 13 observation points to reconstruct a straight line segment $a(t) = (0, 0, t - 2)$ with $t \in [1, 3]$ in Example 1 and 9 observation points to reconstruct an arc $a(t) = (0, \cos t, \sin t)$ with $t \in [0, \pi]$ in Example 2, respectively. The reconstructed slice and iso-surface are shown in Figs.12 and 13, where it is evident that the trajectories are enclosed by the intersections of the smallest annulus $\Lambda_\Gamma^{(x_j)}$ centered at x_j and containing their own trajectories. However, since we have only chosen a partial set of observation points, we are not able to reconstruct the trajectories perfectly.

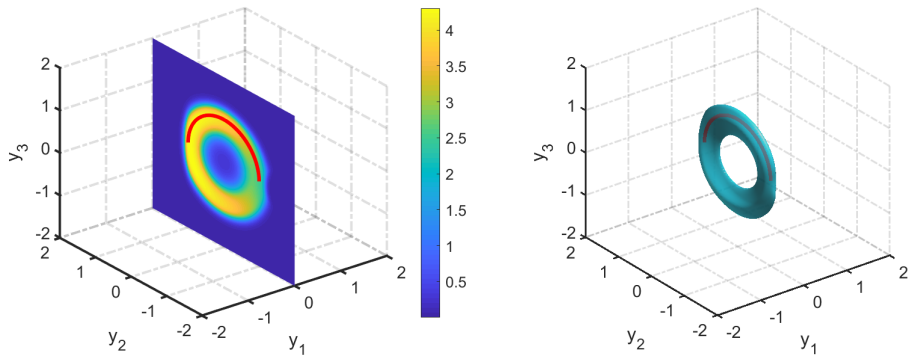

(a) A slice at $y_1 = 0$ (b) Iso-surface level = 1

Figure 13: Reconstruction from sparse observation points $x = (2\sin\varphi\cos\theta, 2\sin\varphi\sin\theta, 2\cos\varphi)$ with $\theta \in [0, 2\pi)$ and $\varphi = \pi/2$ for an arc $a(t) = (0, \cos t, \sin t)$ where $t \in [0, \pi]$. Here $M = 9$ denotes the number of the observation points and we take $\theta = \pi + (j-1)\pi/8$, $j = 1, \cdots, M$ and $\varphi = \pi/2$ such that $A_\Gamma^{(x_j)} = \Lambda_\Gamma^{(x_j)}$.

Next, assuming that all the selected observation points may contain both observable and non-observable points. In the presented numerical examples below, we set the threshold value as $M' = 5 \times 10^2$. Figs.14 and 15 demonstrate the reconstructed trajectory for orbit functions $a(t) = (0, 0, t-2)$ with $t \in [1, 3]$ using sparse observation points and varying frequency bandwidths. Although sparse observation points data are used, the trajectory cannot be fully determined from Figs.14 and 15. When $M = 4, 6, 13$, there always exist observation points x_j such that $A_\Gamma^{(x_j)} \subset \Lambda_\Gamma^{(x_j)}$ similar to Fig.6. For such observation points, reconstructed annulus $A_\Gamma^{(x_j)}$ may be too narrow and the intersections of the annulus $A_\Gamma^{(\hat{x}_j)}$ can only reveal the starting and ending points of the trajectory of the moving point source. Figs.16 and 17 illustrate visualizations of the reconstructed trajectory for orbit functions $a(t) = (0, \cos t, \sin t)$ with $t \in [0, \pi]$ and varying frequency bandwidths using sparse observation points. The starting and ending points of the arc trajectory can be determined from these visualizations.

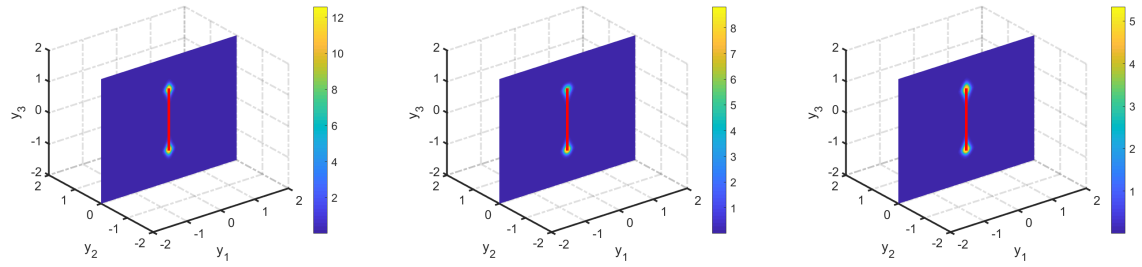

(a) $M = 4$ (b) $M = 6$ (c) $M = 13$

Figure 14: Reconstruction from sparse observation points $x = (2\sin\varphi\cos\theta, 2\sin\varphi\sin\theta,\ 2\cos\varphi)$ with $\theta \in [0, 2\pi)$ and $\varphi \in [0, \pi]$ for a straight line segment $a(t) = (0, 0, t-2)$ where $t \in [1, 3]$. Here M denotes the number of the observation points. (a) $\theta = (j-1) * 2\pi/4$, $j = 1, \cdots, 4$ and $\varphi = \pi/2$; (b) $\varphi = 0$; $\theta = (j-1) * 2\pi/4$, $j = 1, \cdots, 4$ and $\varphi = \pi/2$; $\varphi = \pi$; (c) $\theta = (2j-1) * \pi/4$, $j = 1, \cdots, 4$, $\varphi = \pi/3$; $\theta = (j-1) * 2\pi/4$, $j = 1, \cdots, 4$, $\varphi = \pi/2$; $\theta = j * 2\pi/3$, $j = 1, \cdots, 5$, $\varphi = 2\pi/3$.

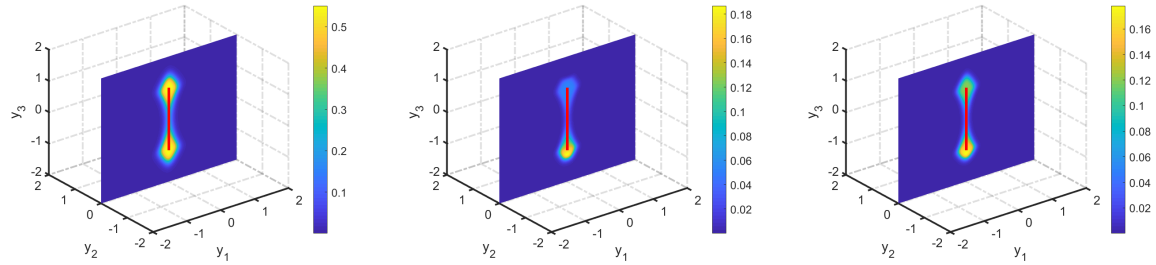

(a) $M = 4$ (b) $M = 6$ (c) $M = 13$

Figure 15: Reconstruction from sparse observation points $x = (2\sin\varphi\cos\theta, 2\sin\varphi\sin\theta,\ 2\cos\varphi)$ with $\theta \in [0, 2\pi)$ and $\varphi \in [0, \pi]$ for a straight line segment $a(t) = (0, 0, t-2)$ where $t \in [1, 3]$. Here M denotes the number of the observation points. (a) $\theta = (j-1) * 2\pi/4$, $j = 1, \cdots, 4$ and $\varphi = \pi/2$; (b) $\varphi = 0$; $\theta = (j-1) * 2\pi/4$, $j = 1, \cdots, 4$ and $\varphi = \pi/2$; $\varphi = \pi$; (c) $\theta = (2j-1) * \pi/4$, $j = 1, \cdots, 4$, $\varphi = \pi/3$; $\theta = (j-1) * 2\pi/4$, $j = 1, \cdots, 4$, $\varphi = \pi/2$; $\theta = j * 2\pi/3$, $j = 1, \cdots, 5$, $\varphi = 2\pi/3$. We take $k_{min} = 1$ and $k_{max} = 5$.

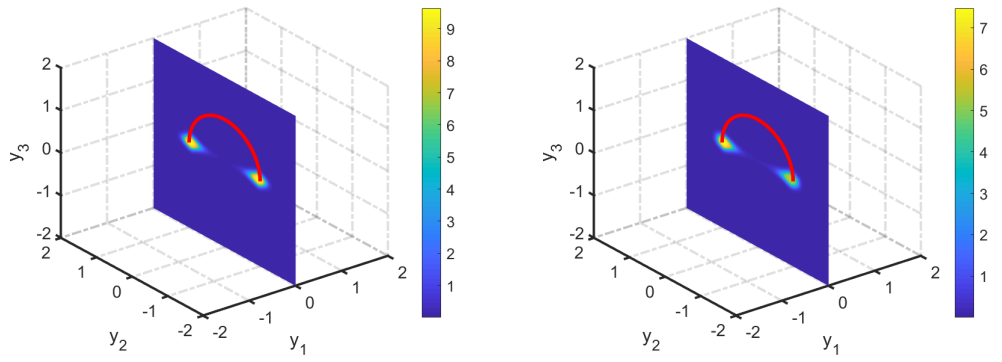

(a) $M = 4$ (b) $M = 6$

Figure 16: Reconstruction from sparse observation points $x = (2\sin\varphi\cos\theta, 2\sin\varphi\sin\theta,\ 2\cos\varphi)$ with $\theta \in [0, 2\pi)$ and $\varphi \in [0, \pi]$ for a straight line segment $a(t) = (0, \cos t, \sin t)$ where $t \in [0, \pi]$. Here M denotes the number of the observation points. (a) $\theta = (j-1) * 2\pi/4$, $j = 1, \cdots, 4$ and $\varphi = \pi/2$; (b) $\theta = (j-1) * 2\pi/4$, $j = 1, \cdots, 4$ and $\varphi = \pi/2$; $\varphi = 0$; $\varphi = \pi$.

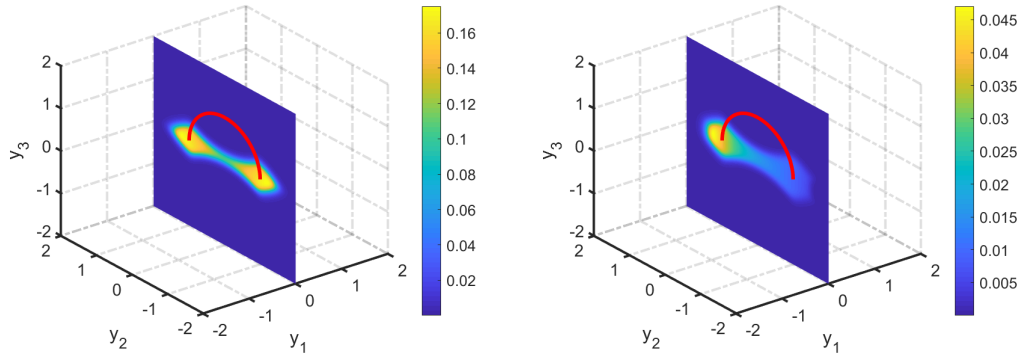

(a) $M = 4$ (b) $M = 6$

Figure 17: Reconstruction from sparse observation points $x = (2\sin\varphi\cos\theta, 2\sin\varphi\sin\theta,\ 2\cos\varphi)$ with $\theta \in [0, 2\pi)$ and $\varphi \in [0, \pi]$ for a straight line segment $a(t) = (0, \cos t, \sin t)$ where $t \in [0, \pi]$. Here M denotes the number of the observation points. (a) $\theta = (j-1) * 2\pi/4$, $j = 1, \cdots, 4$ and $\varphi = \pi/2$; (b) $\theta = (j-1) * 2\pi/4$, $j = 1, \cdots, 4$ and $\varphi = \pi/2$; $\varphi = 0$; $\varphi = \pi$. We take $k_{min} = 1$ and $k_{max} = 5$.

Finally, we aim to reconstruct the trajectories of a straight line segment and an arc using uniformly distributed observation points on a sphere with a radius of 2. We consider sets of 20, 30, and 40 points for this purpose. Fig.18 displays the location of the 40 uniformly distributed points. While increasing the number of observation points, Fig.19 and 20 demonstrate that only the starting and ending points of the trajectories can be determined. This limitation is a result

of the observation points in the observable set with $A_\Gamma^{(x)} \subset \Lambda_\Gamma^{(x)}$.

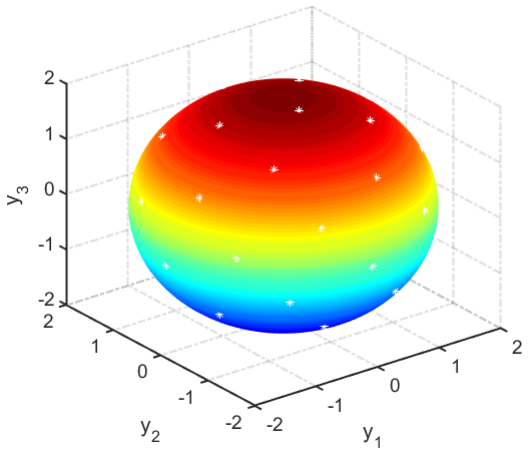

Figure 18: 40 uniformly distributed points on a sphere with a radius of 2.

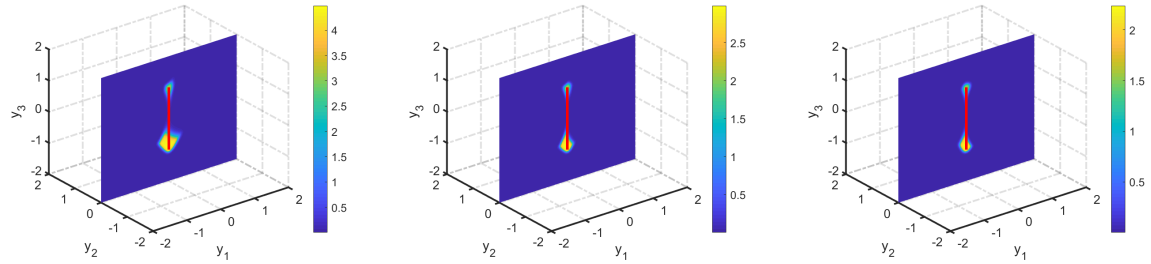

(a) $M = 20$ (b) $M = 30$ (c) $M = 40$

Figure 19: Reconstruction from sparse uniformly distributed observation points on a sphere with a radius of 2 for a straight line segment $a(t) = (0, 0, t-2)$ where $t \in [1, 3]$. Here we take different numbers of observation points M.

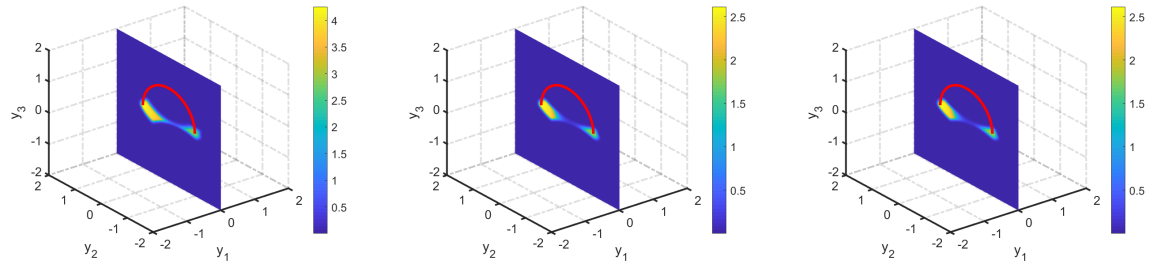

(a) $M = 20$ (b) $M = 30$ (c) $M = 40$

Figure 20: Reconstruction from sparse uniformly distributed observation points on a sphere with a radius of 2 for an arc $a(t) = (0, \cos t, \sin t)$ where $t \in [0, \pi]$. Here we take different numbers of observation points M.

5.3 Noisy test

We evaluate sensitivity with respect to the noisy data by selecting Example 1, which involves a line segment recovery. The near-field data are corrupted with Gaussian noise, as shown below:

$$w_\delta(x,k) \coloneqq \mathrm{Re}\left[w(x,k)\right]\left(1+\delta\,\gamma_1\right) + i\mathrm{Im}[w(x,k)]\left(1+\delta\,\gamma_2\right)$$

where $\delta > 0$ represents the noise level and $\gamma_j \in [-1,1]$ $(j = 1,2)$ denote Gaussian random variables.

To accomplish this test, we assigned $\delta = 5\%, 10\%, 15\%, 20\%$ and plot the indicator functions in Figs.21 and 22 using one and sparse observation points, respectively. The images are clearly getting distorted at higher noise levels, but the starting and the ending points of the trajectory of the moving source using the data measured at sparse points can still be well-captured. A reconstruction in the noise-free case is not presented since the effectiveness is demonstrated in the other examples.

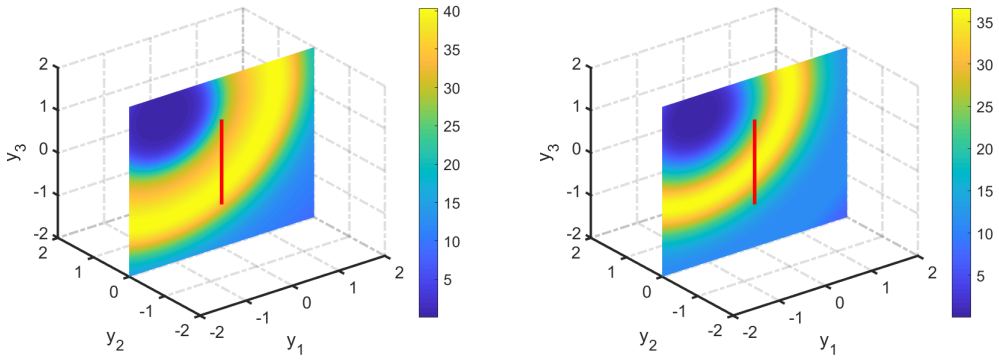

(a) $\delta = 5\%$

(b) $\delta = 10\%$

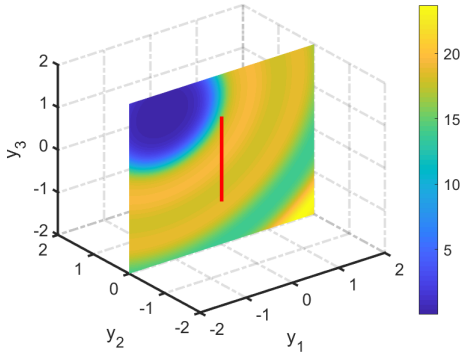

(c) $\delta = 15\%$

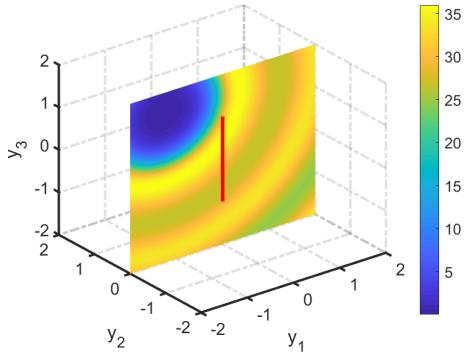

(d) $\delta = 20\%$

Figure 21: Reconstruction of a straight line segment $a(t) = (0, 0, t - 2)$, $t \in [1, 3]$ from noisy data with different levels δ measured at a single observable point $x = (2 \sin\varphi \cos\theta, 2 \sin\varphi \sin\theta, 2 \cos\varphi)$ with $\theta = \pi$ and $\varphi = 2\pi/9$.

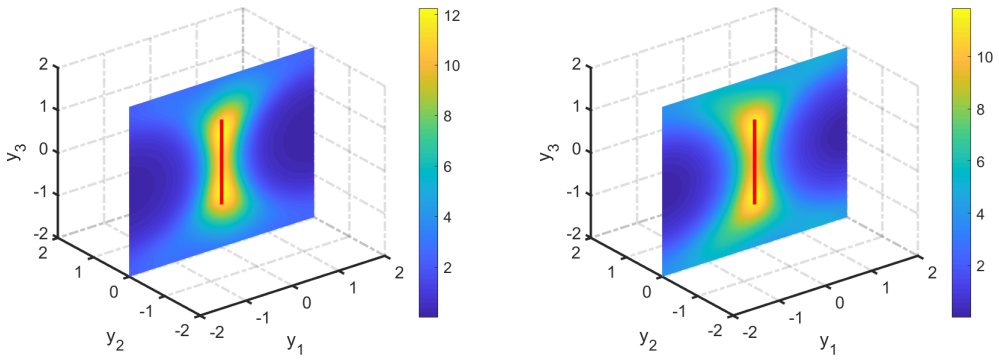

(a) $\delta = 5\%$ (b) $\delta = 10\%$

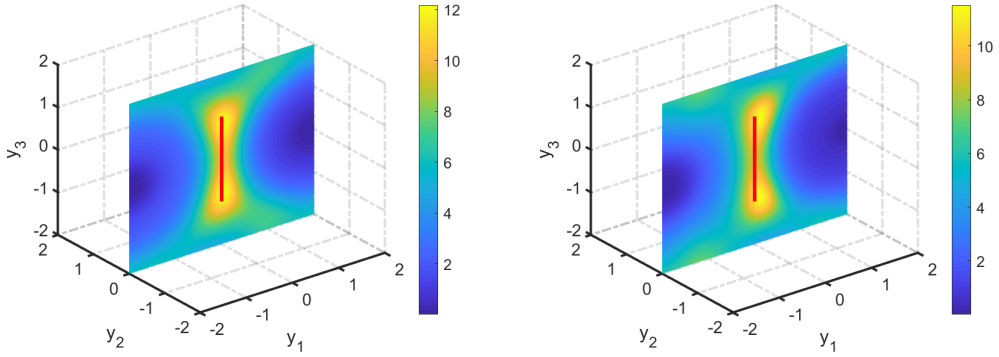

(c) $\delta = 15\%$ (d) $\delta = 20\%$

Figure 22: Reconstruction of a straight line segment $a(t) = (0, 0, t-2)$, $t \in [1, 3]$ from noisy data with different levels δ measured at sparse observable point $x = (2\sin\varphi\cos\theta, 2\sin\varphi\sin\theta, 2\cos\varphi)$ with $\theta = 0, \pi/2, \pi, 3\pi/2$ and $\varphi = \pi/2$.

Acknowledgements

G. Hu is partially supported by the National Natural Science Foundation of China (No. 12071236) and the Fundamental Research Funds for Central Universities in China (No. 63213025).

References

[1] A. Alzaalig, G. Hu, X. Liu and J. Sun, Fast acoustic source imaging using multi-frequency sparse data, Inverse Problems, 36 (2020): 025009.

[2] B. Chen, Y. Guo, F. Ma and Y. Sun, Numerical schemes to reconstruct three-dimensional time-dependent point sources of acoustic waves, Inverse Problems, 36 (2020): 075009.

[3] M. Cheney and B. Borden, Imaging moving targets from scattered waves, Inverse Problems 24 (2008): 035005.

[4] J. Cooper, Scattering of plane waves by a moving obstacle. Arch. Ration. Mech. Anal. 71 (1979): 113-149.

[5] J. Cooper and W. Strauss, Scattering of waves by periodically moving bodies. J. Funct. Anal. 47 (1982): 180-229.

[6] J. Fournier, J. Garnier, G. Papanicolaou and C. Tsogka, Matched-filter and correlation-based imaging for fast moving objects using a sparse network of receivers, SIAM J. Imag. Sci., 10 (2017): 2165-2216.

[7] J. Garnier and M. Fink, Super-resolution in time-reversal focusing on a moving source, Wave Motion, 53 (2015): 80-93.

[8] R. Griesmaire and C. Schmiedecke, A Factorization method for multifrequency inverse source problem with sparse far field measurements, SIAM J. Imag. Sci., 10 (2017): 2119-2139.

[9] R. Griesmarier, H. Guo, G. Hu, Inverse wave-number-dependent source problems for the Helmholtz equation, in preparing.

[10] H. Guo, G. Hu and M. Zhao, Direct sampling method to inverse wave-number-dependent source problems (part I): determination of the support of a stationary source, arXiv:2212.04806.

[11] G. Hu, Y. Kian, P. Li and Y. Zhao, Inverse moving source problems in electrodynamics, Inverse Problems, 35 (2019): 075001.

[12] G. Hu, Y. Kian and Y. Zhao, Uniqueness to some inverse source problems for the wave equation in unbounded domains, Acta Mathematicae Applicatae Sinica, English Series, 36 (2020): 134-150.

[13] G. Hu, Y. Liu and M. Yamamoto, Inverse moving source problem for fractional diffusion(-wave) equations: Determination of orbits, Inverse Problems and Related Topics ed J Cheng, S Lu and M Yamamoto (Singapore: Springer) pp. 81-100, 2020.

[14] V. Isakov, Inverse Source Problems, AMS, Providence, RI, 1989.

[15] H. A. Jebawy, A. Elbadia and F. Triki, Inverse moving point source problem for the wave equation, Inverse Problems, 38 (2022): 125003.

[16] A. Kirsch and N. Grinberg, The Factorization Method for Inverse Problems, Oxford University Press, Oxford, UK, 2008.

[17] Y. Liu, Y. Guo, and J. Sun, A deterministic-statistical approach to reconstruct moving sources using sparse partial data, Inverse Problems, 37 (2021): 065005.

[18] Y. Liu, G. Hu and M. Yamamoto, Inverse moving source problem for time-fractional evolution equations: determination of profiles, Inverse Problems, 37 (2021): 084001.

[19] Y. Liu, Numerical schemes for reconstructing profiles of moving sources in (time-fractional) evolution equations, RIMS Kokyuroku 2174 (2021): 73-87.

[20] E. Nakaguchi, H. Inui and K. Ohnaka. An algebraic reconstruction of a moving point source for a scalar wave equation, Inverse Problems, 28 (2012): 065018.

[21] T. Ohe, H. Inui and K. Ohnaka, Real-time reconstruction of time-varying point sources in a three-dimensional scalar wave equation. Inverse Problems, 27 (2011): 115011.

[22] P. D. Stefanov, Inverse scattering problem for moving obstacles, Math. Z. 207 (1991): 461-480.

[23] J. Sylvester and J. Kelly, A scattering support for broadband sparse near-field measurements, Inverse Problems, 21 (2005): 759-771.

[24] O. Takashi. Real-time reconstruction of moving point/dipole wave sources from boundary measurements, Inverse Probl. Sci. Eng., 28 (2020): 1057-1102.

[25] S. Wang, Mirza Karamehmedovic, Faouzi Triki, Localization of moving sources: uniqueness, stability and Bayesian inference, arXiv:2204.04465.